Atmos. Meas. Tech. Discuss., 6, 6873–6933, 2013
www.atmos-meas-tech-discuss.net/6/6873/2013/
doi:10.5194/amtd-6-6873-2013

Atmospheric Measurement Techniques
Discussions
Open Access

This discussion paper is/has been under review for the journal Atmospheric Measurement Techniques (AMT). Please refer to the corresponding final paper in AMT if available.

Kalman filter physical retrieval of geophysical parameters from high temporal resolution geostationary infrared radiances: the case of surface emissivity and temperature

G. Masiello[1], C. Serio[1], I. De Feis[2], M. Amoroso[1], S. Venafra[1], I. F. Trigo[3], and P. Watts[4]

[1]Scuola di Ingegneria, Università della Basilicata, Potenza, Italy
[2]Istituto per le Applicazioni del Calcolo "Mauro Picone" (CNR), Napoli, Italy
[3]Instituto Portugues do Mar e da Atmosfera IP, Land SAF, Lisbon, Portugal
[4]EUMETSAT, Darmstadt, Germany

Received: 7 July 2013 – Accepted: 8 July 2013 – Published: 26 July 2013

Correspondence to: C. Serio (carmine.serio@unibas.it)

Published by Copernicus Publications on behalf of the European Geosciences Union.

Abstract

The high temporal resolution of the data acquisition by geostationary satellites and their capability to resolve the diurnal cycle are a precious source of information which could be suitably used to retrieve geophysical parameters. Currently this information is for the most part considered as uncorrelated, both in space and time: each pixel is treated independently from its neighbors and the present events are not linked to past or future ones. In this paper we develop a Kalman filter approach to apply spatial and temporal constraints to estimate the geophysical parameters from radiance measurements made from geostationary platforms. We apply the new strategy to a particular case study, i.e. the retrieval of emissivity and surface temperature from SEVIRI (Spinning Enhanced Visible and InfraRed Imager) observations over a target area encompassing the Iberian Peninsula and Northwestern Africa. The retrievals are then compared with in situ data, and other similar satellite products.

1 Introduction

Infrared instrumentation on geostationary satellites is now rapidly approaching the spectral quality and accuracy of modern sensors flying on polar platforms. Currently at the core of European Organisation for the Exploitation of Meteorological Satellites (EUMETSAT) geostationary meteorological programme is the Meteosat Second Generation (MSG). However EUMETSAT is preparing for Meteosat Third Generation (MTG) which will carry on board the Flexible Combined Imager (FCI) having a spatial resolution of 1–2 km at the sub-satellite point, 16 channels (8 in the thermal band) and the Infrared Sounder (IRS) that will be able to provide unprecedented information on horizontally, vertically, and temporally (4-dimensional) resolved water vapour and temperature structures of the atmosphere. It will have a hyperspectral resolution of 0.625 cm^{-1} wave-number, taking measurements in two bands, the Long-Wave InfraRed (LWIR)

AMTD
6, 6873–6933, 2013

Geophysical parameters retrieval from geostationary platforms

G. Masiello et al.

(14.3–8.3 µm) and the Mid-Wave InfraRed (MWIR) (6.25–4.6 µm), with a spatial resolution of 4 km and with a basic repeat cycle of 60 min.

The capability of geostationary satellites to resolve the diurnal cycle and hence to provide time-resolved sequences or times series of observations is a source of information which could suitably constrain the derivation of geophysical parameters. Nowadays, also because of lack of time-continuity, when dealing with observations from polar platforms, the problem of deriving geophysical parameters is normally accomplished by considering each single observation as independent from past and future events. For historical reasons, the same approach is currently generally pursued with geostationary observations, i.e. dealt with as if they were polar observations.

The fact that time continuity of the observations brings much information about atmospheric processes is normally evidenced by the pronounced dynamical correlation, which in many instances can be modeled with Markov chains or Markov stochastic processes (e.g., Serio, 1992, 1994; Cuomo et al., 1994, and references therein).

In this paper we present a Kalman filter methodology that incorporates dynamical correlation within the retrieval process without making use of a full dynamical Numerical Weather Prediction (NWP) system, because the objective of our study has been to get better insight into understanding how we can have a better exploitation of satellite data per se, in other words the analysis moves within a context, which envisages an almost entirely data-driven system.

The issue of using dynamical correlation or evolution of the observations call for state or evolutionary equations, which can be modeled with simply stochastic recursive equations. This brings us inevitably to the Kalman filter (e.g., Kalman, 1960; Kalman and Bucy, 1961; Nychka and Anderson, 2010). With the Kalman filter (KF) we can introduce time constraint via a suitable dynamical system, which describes how the given atmospheric state vector evolves over time. It is important to stress that the dynamical system is mostly used to convey within the estimation process time-space information, which, within the Gaussian assumption, is normally done in terms of first and second order statistics: mean and covariance matrices.

Discussion Paper | Discussion Paper | Discussion Paper | Discussion Paper |

AMTD

6, 6873–6933, 2013

Geophysical parameters retrieval from geostationary platforms

G. Masiello et al.

Since KF has the Markov property (Nychka and Anderson, 2010), the current update or estimation of state vector depends only on the current state (a-priori information) and the observations. In other words, unless we want to make predictions (that is to make forecasts much ahead than the current state), the precise form of the evolutionary equation is not important for the estimation problem, but the current state and its statistics. When we focus on the current update or estimation of the state vector, KF is formally equivalent to the Rodgers' Optimal Estimation (Rodgers, 2000), where the current state plays the role, as said, of a-priori information (although it has to be stressed that a substantial difference is that in Rodgers' Optimal Estimation the a-priori covariance is not propagated based on the dynamics).

The KF methodology will be exemplified for the problem of surface temperature-emissivity ($[T_s, \epsilon]$) separation, that is the simultaneous retrieval of $[T_s, \epsilon]$ from SEVIRI infrared channels. Toward this objective, a case study has been defined, which includes a specific target area characterized by a large variety of surface features.

The results from this case study have been inter-compared with those obtained by IASI (Infrared Atmospheric Sounder Interferometer), for the same target area and dates, in a recent paper by Masiello and Serio (2013). The inter-comparison showed that SEVIRI and IASI products for temperature agree with within 1 K, whereas emissivity retrievals are found highly consistent with differences, which normally are of the order of ≈ 0.001.

The present study mainly focuses on the KF methodology and comparison of its results with in situ data, and other similar satellite products, such as AVHRR (Advanced Very High Resolution Radiometer). According to the most recent review on the subject of $[T_s, \epsilon]$ retrieval from satellite observations (Li et al., 2013), our KF-approach from geostationary platform is novel. A similarity could be found with the scheme developed by Li et al. (2011). However, while in (Li et al., 2011) the observations are accumulated for a prescribed time slot (normally six hours), we pursue a genuine dynamical strategy, which exploits the sequential approach of the Kalman filter. This results in an algorithm, which does not need to increase the dimensionality of the data space because of time accumulation, while preserving the highest time resolution prescribed by the repeat time of the geostationary instrumentation (15 min for SEVIRI).

The study is organized as follows. Section 2 will present the data used in the analysis. This section will also provide some details about the forward model we have developed for SEVIRI. Section 3 will deal with the retrieval methodology, whereas Sect. 4 will exemplify the application of the methodology to a SEVIRI case study. Finally, conclusions will be made in Sect. 5.

2 Data and forward modelling

2.1 Data

The KF methodology we are going to show in this paper will be exemplified for a particular case study, which involves the retrieval of emissivity and surface temperature from SEVIRI infrared channels in the atmospheric window over a target area, covering a geographic region with very different surface features: sea water, arid, vegetated and cultivated land, urban areas.

The Spinning Enhanced Visible and InfraRed Imager (SEVIRI) on board Meteosat-9 (Meteorological Satellite-9) allows for a complete image scan (Full Earth Scan) once every 15 min period with a spatial resolution of 3 km for 12 channels (8 in the thermal band), over the full disk covering Europe, Africa and part of South America.

SEVIRI infrared channels range from 12 µm to 3.9 µm. Their conventional definition in terms of channel number is given in Table 1, whereas their spectral response is shown in Fig. 1. The figure also provides a comparison with a typical IASI spectrum at a spectral sampling of 0.5 cm^{-1}.

IASI has been developed in France by the Centre National d'Etudes Spatiales (CNES) and is flying on board the Metop (Meteorological Operational Satellite) platform, a series of three satellites of the European Organization for the Exploitation of Meteorological Satellite (EUMETSAT) European Polar System (EPS). The instrument

AMTD
6, 6873–6933, 2013

has a spectral coverage extending from 645 to 2760 cm^{-1}, which with a sampling interval $\Delta\sigma = 0.25\,cm^{-1}$ gives 8461 data points or channels for each single spectrum. Data samples are taken at intervals of 25 km along and across track, each sample having a minimum diameter of about 12 km. Further details on IASI and its mission objectives can be found in Hilton et al. (2012). Atmospheric parameters (temperature, water vapour and ozone profiles) derived from IASI spectral radiances will be used in this paper to assess the sensitivity of SEVIRI atmospheric window infrared channels to the atmospheric state vector.

As said before, for the purpose of this study, SEVIRI Meteosat-9 highrate level 1.5 image data and IASI (level 1C) observations have been collected for the target area shown in Fig. 2 for the full month of July 2010. The area is covered with 392088 Meteosat-9 pixels and includes Spain, Portugal, and part of the North-West Africa, and the Western part of the Mediterranean Basin.

To check the performance of the scheme, we have also selected three smaller areas (also shown in Fig. 2 with red boxes) in Spain, Sahara desert and the Mediterranean Basin, which have size $0.5^\circ \times 0.5^\circ$ (lat, lon) and correspond each to one box of the ECMWF (European Centre for Medium Range Weather Forecasts) analysis grid mesh (see, e.g. Fig. 3). For the Spanish location the area includes 187 SEVIRI pixels, 219 for the Sahara desert and 178 for the Mediterranean Basin. The land coverage for the small target area close to Seville is a mosaic of cultivated areas, with green grass, foliage, bare soil and urban areas. For this type of coverage we expect an emissivity at atmospheric window well above 0.90. The small Sahara desert area is just a desert sand homogeneous flat area, with no vegetation. In this case we know that emissivity is dominated by quartz particles, which yield a characteristic fingerprint at 8.6 µm (reststrhalen doublet of quartz). This strong signature is in the middle of the SEVIRI channel at 8.7 µm, and, therefore, the retrieved emissivity at this channel has to show the quartz fingerprint.

For the whole target area shown in Fig. 2, we have also acquired ancillary information for the characterization of the thermodynamical atmospheric state. This information is

AMTD
6, 6873–6933, 2013

Geophysical parameters retrieval from geostationary platforms

G. Masiello et al.

provided by ECMWF analysis products for the surface temperature, T_s and the atmospheric profiles of temperature, water vapour and ozone $[T, Q, O]$ at the canonical hours 0:00, 6:00, 12:00 and 18:00 UTC. ECMWF model data are provided on $0.5 \times 0.5^\circ$ (lat, lon) grid. In each ECMWF grid box there are on average ≈ 200 SEVIRI pixels, for which we assume that the atmospheric state vector is the time co-located ECMWF analysis (e.g. see Fig. 3).

Within the inverse scheme, an important issue concerns the background vector and covariance matrix for emissivity. For the purpose of developing a suitable background for emissivity, we have used the University of Wisconsin (UW) Baseline Fit (BF) Emissivity database (UW/BFEMIS data base, e.g. http://cimss.ssec.wisc.edu/iremis/) (Seemann et al., 2008; Borbas and Ruston, 2010).

UW/BFEMIS database is available from year 2003 to 2012 globally with 0.05° spatial resolution. Details of how to transform UW/BFEMIS data base emissivity to SEVIRI channel emissivity can be found in Serio et al. (2013); Masiello et al. (2013). Derived from the UW/BFEMIS data base, the SEVIRI channel emissivity data have been used to build up an appropriate a-priori or background (mean value and covariance) for the retrieval algorithm.

For the purpose of comparison, we have used also NOAA (National Ocean and Atmosphere Administration) optimum interpolation $1/4^\circ$ daily sea surface temperature analysis for the month of July 2010. The analysis, which is a product of the processing of AMSR (Advanced Microwave Scanning Radiometer) and AVHRR (Advanced Very High Resolution Radiometer), will be compared to that obtained by SEVIRI for sea surface. The analysis will be referred to as AMSR+AVHRR OISST in the remainder of this paper. The AMSR+AVHRR OISST analysis has been downloaded from the web site ftp://eclipse.ncdc.noaa.gov/pub/OI-daily-v2/NetCDF/2010/AVHRR-AMSR/.

Finally, we have also used data collected at Evora ground site (38.55° N, 8.01° W) located in Southern Portugal and maintained by the EUMETSAT Satellite Applications Facility on Land Surface Analysis (LSA SAF) team. The area surrounding the site is dominated by Quercus woodland plains and is fairly homogeneous at the SE-

AMTD
6, 6873–6933, 2013

Geophysical parameters retrieval from geostationary platforms

G. Masiello et al.

VIRI spatial scales (Dash et al., 2004). The ground station is equipped with a suite of radiometers (9.6–11.5 µm range) providing temperatures of tree canopies and of shadowed and sunlit ground. These are combined to provide a composite ground temperature representative of SEVIRI pixel, considering that the fractional area coverage of canopies is 0.32 (Trigo et al., 2008). It is worth mentioning that ground and tree top canopy present contrasting temperatures particularly during daytime, when differences can easily reach 15 K. As a consequence, the composite ground temperatures are fairly sensitive to the fraction of trees being considered. For this purpose, the area surrounding Evora station was carefully characterized using very high resolution IKONOS images (Kabsch et al., 2008; Trigo et al., 2008). In addition, our Kalman Filter retrievals for the pixel closer to Evora are also compared with the operational land surface temperature product provided by the LSA SAF (Freitas et al., 2010).

2.2 Forward models: σ-IASI and σ-SEVIRI

Forward calculations for the SEVIRI channels 2–8 (see Table 1) are obtained by the σ-SEVIRI code, that we have developed purposely for this study.

We do not consider the SEVIRI channel at 3.9 µm since during daytime it is contaminated by reflected solar radiation and affected by non local thermodynamic equilibrium (non-LTE) effects. Furthermore, the CO_2 line mixing at 4.3 µm CO_2 band head is poorly modeled in state-of-art radiative transfer, which can add potentially large bias.

Regarding channels 2 to 8, the forward model, σ-SEVIRI has been derived from σ-IASI (Amato et al., 2002), which is a monochromatic radiative transfer designed for the fast computation of spectral radiance and its derivatives (Jacobian) with respect to a given set of geophysical parameters.

The form of the radiative transfer equation, which σ-IASI and hence σ-SEVIRI consider in its numerical scheme, has been recently reviewed and presented in Masiello and Serio (2013), which the interested reader is referred to. The model also takes into account the radiance term which is reflected from the surface back to the satellite. Both Lambertian and specular reflections can be modeled.

AMTD
6, 6873–6933, 2013

To accomplish the radiative transfer calculation σ-IASI uses a look-up table for the optical depth, which has been developed from one of the most popular line-by-line forward models, LBLRTM (Clough et al., 2005).

The model σ-SEVIRI is itself based on a look-up table, which is obtained by a proper down-sampling of the look-up table for σ-IASI. For this reason we need to give some details about σ-IASI in order to describe how σ-SEVIRI works.

The σ-IASI model (Amato et al., 2002) parameterizes the monochromatic optical depth with a second order polynomial. At a given pressure-layer and wave number, σ (in cm^{-1} units), the optical depth for the a generic i-th molecule, is computed according to

$$\chi_{\sigma,i} = q_i \left(c_{\sigma,0,i} + c_{\sigma,1,i} T + c_{\sigma,2,i} T^2 \right) \tag{1}$$

where T is the temperature, q_i the molecule concentration and $c_{\sigma,j,i}$ with $j = 0,1,2$, are fitted coefficients, which are actually stored in the optical depth look-up-table.

Unlike other gases, for water vapour, in order to take into account effects depending on the gas concentration, such as self-broadening, a bi-dimensional look-up-table is used Masiello and Serio (2003). Thus, for water vapour, identified with $i = 1$, the optical depth is calculated according to

$$\chi_{\sigma,1} = q_1 \left(c_{\sigma,0,1} + c_{\sigma,1,1} T + c_{\sigma,2,1} T^2 + c_{\sigma,3,1} q_1 \right) \tag{2}$$

The subscript σ indicates the monochromatic quantities. In the case of hyperspectral instrument, such as IASI, the monochromatic optical depths are computed and parameterized at the spectral sampling interval of $10^{-4}\,cm^{-1}$.

This spectral sampling is too much fine for a band instrument such as SEVIRI. In the case of SEVIRI the spectral sampling can be averaged and sampled at a rate of $10^{-1}\,cm^{-1}$ without sacrificing accuracy. Also in this case the optical depth can be parameterized with a low order polynomial and its coefficients are obtained as explained below.

Discussion Paper | Discussion Paper | Discussion Paper | Discussion Paper |

AMTD
6, 6873–6933, 2013

Geophysical parameters retrieval from geostationary platforms

G. Masiello et al.

For each species i we can define an equivalent optical depth $\chi_{\langle\sigma\rangle,i}$, which can be parameterized with respect to temperature in the same way we do for monochromatic quantities (Eqs. 1 and 2).

In the following of this section the angular brackets, $\langle\cdot\rangle$ will be used to indicate the average operation over the wave number.

The equivalent optical depth is

$$\chi_{\langle\sigma\rangle,i} = q_i \left(c_{\langle\sigma\rangle,0,i} + c_{\langle\sigma\rangle,1,i}T + c_{\langle\sigma\rangle,2,i}T^2\right) \tag{3}$$

where the equivalent coefficients $c_{\langle\sigma\rangle,j,i}$ with $j = 0,1,2$, are obtained by fitting the layer transmittance averaged over the coarse sampling of 10^{-1} cm^{-1}.

$$\begin{aligned} q_i \left(c_{\langle\sigma\rangle,0,i} + c_{\langle\sigma\rangle,1,i}T + c_{\langle\sigma\rangle,2,i}T^2\right) &= -\log\left(\langle\tau_{\sigma,i}\rangle\right) \\ &= -\log\left[\langle\exp\left(-\chi_{\sigma,i}\right)\rangle\right] \end{aligned} \tag{4}$$

Because of this down-sampling σ-SEVIRI, which is based on the coarse-mesh look up table, runs ≈ 1000 times faster that σ-IASI.

As the parent code, σ-IASI, σ-SEVIRI can compute the analytical jacobian derivative for a large set of surface and atmospheric parameters: ϵ, T_s and $[T,Q,O]$.

3 The retrieval framework

Before showing the retrieval problem for the couple of surface parameters, emissivity-temperature ($[T_\mathrm{s},\epsilon]$), we briefly review the concept of the optimal estimation in the general context of data assimilation (Wikle and Berliner, 2007), which allows us to describe the retrieval methodology in its general spatio-temporal framework and also to put in evidence its commonalities with the KF methodology.

For the benefit of the reader, we will try to stay as much as possible close to the notation used in Rodgers (2000), therefore the symbol and subscript ε will be used to denote the observational covariance matrix, hence, the noise term affecting the spectral radiance. For emissivity we will use the symbol ϵ, which should not be confused with ε.

3.1 Static a-priori background

To simplify the exposition let us assume that the times are indexed by integers, $t = 1, 2, \ldots$, although handling uneven spaced times does not add any fundamental difficulty.

The derivation of the thermodynamical state of the atmosphere, at a given time t given a set of independent observations of the spectral radiance, $R_t(\sigma)$, is well established when each time t is considered independent from past and future measures. Indeed assuming

$$\mathbf{R}_t = (R_t(\sigma_1), \ldots, R_t(\sigma_M))^{\mathrm{T}} \tag{5}$$

and under the assumption of multivariate normality the retrieval problem can be seen as one of variational analysis in which a suitable estimation of the state vector is obtained by minimizing the form (see e.g. Carissimo et al., 2005; Courtier, 1997; Talagrand, 1997; Tarantola, 1987)

$$\min_{\boldsymbol{v}} \frac{1}{2}(\mathbf{R}_t - F(\boldsymbol{v}))^{\mathrm{T}} \mathbf{S}_\varepsilon^{-1} (\mathbf{R}_t - F(\boldsymbol{v})) + \frac{1}{2}(\boldsymbol{v} - \boldsymbol{v}_{\mathrm{a}}))^{\mathrm{T}} \mathbf{S}_{\mathrm{a}}^{-1} (\boldsymbol{v} - \boldsymbol{v}_{\mathrm{a}})) \tag{6}$$

where

N: is the number of atmopsheric parameters to beretrieved (7)

M: is the number of spectral radiances

F: is the forward model function

$\boldsymbol{v}$: is the atmospheric state vector, of size N

$\boldsymbol{v}_{\mathrm{a}}$: is the atmospheric background state vector, of size N

AMTD
6, 6873–6933, 2013
Geophysical parameters retrieval from geostationary platforms
G. Masiello et al.

$\mathbf{S}_\varepsilon$: is the observational covariance matrix, of size $M \times M$

$\mathbf{S}_\mathrm{a}$: is the background covariance matrix, of size $N \times N$

Equation (6) is commonly linearized and a Gauss Newton iterative method is used to solve the quadratic form

$$\min_{\boldsymbol{x}} \frac{1}{2}(\boldsymbol{y}_t - \mathbf{K}\boldsymbol{x})^\mathrm{T} \mathbf{S}_\varepsilon^{-1} (\boldsymbol{y}_t - \mathbf{K}\boldsymbol{x}) + \frac{1}{2}(\boldsymbol{x} - \boldsymbol{x}_\mathrm{a})^\mathrm{T} \mathbf{S}_\mathrm{a}^{-1} (\boldsymbol{x} - \boldsymbol{x}_\mathrm{a}) \tag{8}$$

where

$$\mathbf{K} = \frac{\partial F(\boldsymbol{v})}{\partial \boldsymbol{v}}\Big|_{\boldsymbol{v}=\boldsymbol{v}_\mathrm{o}}; \quad \boldsymbol{y}_t = \mathbf{R}_t - \mathbf{R}_\mathrm{ot} \tag{9}$$

$$\boldsymbol{x} = \boldsymbol{v} - \boldsymbol{v}_\mathrm{o}; \qquad \boldsymbol{x}_\mathrm{a} = \mathbf{v}_\mathrm{a} - \boldsymbol{v}_\mathrm{o}$$

It should be stressed that, formally, the state vector, $\boldsymbol{v}$ can be thought of as a 3-D geophysical field, and not necessarily of a vector in one dimension (altitude coordinate).

The formal solution of Eq. (8) is well established (e.g. Tarantola, 1987; Rodgers, 2000)

$$\hat{\boldsymbol{x}} = \boldsymbol{x}_\mathrm{a} + \left(\mathbf{K}^\mathrm{T}\mathbf{S}_\varepsilon^{-1}\mathbf{K} + \mathbf{S}_\mathrm{a}^{-1}\right)^{-1} \mathbf{K}^\mathrm{T}\mathbf{S}_\varepsilon^{-1}(\boldsymbol{y}_t - \mathbf{K}\boldsymbol{x}_\mathrm{a}) \tag{10}$$

$$\hat{\mathbf{S}} = \left(\mathbf{K}^\mathrm{T}\mathbf{S}_\varepsilon^{-1}\mathbf{K} + \mathbf{S}_\mathrm{a}^{-1}\right)^{-1}$$

In the context of *data assimilation*, $\boldsymbol{x}_\mathrm{a}$ is normally the forecast at time, t and $\mathbf{S}_\mathrm{a}$ is the error forecast covariance matrix. The estimation, $\hat{\boldsymbol{x}}$ is referred to as the analysis.

3.2 The Kalman filter

The Kalman filter was first developed by Kalman (1960) and Kalman and Bucy (1961) in an engineering context and as a linear filter. Its derivation within the Bayes formalism has been shown by many authors (e.g. see the review Wikle and Berliner, 2007).

AMTD
6, 6873–6933, 2013

With our notation, the formal filter can be summarized with the couple of equations below, which are often referred to as the *observation equation* (or data model) and the *state equation* (or dynamic model or system model), respectively

$$\begin{cases} \mathbf{R}_t = F(\boldsymbol{v}_t) + \boldsymbol{\varepsilon}_t \\ \boldsymbol{v}_{t+1} = \mathbf{H}\boldsymbol{v}_t + \boldsymbol{\eta}_{t+1} \end{cases} \tag{11}$$

here $\mathbf{H}$ is a linear operator and the noise model term, $\boldsymbol{\eta}_t$ has covariance, $\mathbf{S}_\eta$. The remaining parameters appearing in Eq. (11) have the same meaning as those introduced in Sect. 3.1. KF is intrinsically linear, therefore the observation equation has to be linearized in order to write down the optimal estimation for the state vector. With the same notation we have used until now, we have the linear KF form,

$$\begin{cases} \boldsymbol{y}_t = \mathbf{K}_t\boldsymbol{x}_t + \boldsymbol{\varepsilon}_t \\ \boldsymbol{v}_{t+1} = \mathbf{H}\boldsymbol{v}_t + \boldsymbol{\eta}_{t+1} \end{cases} \tag{12}$$

where we use the notation $\mathbf{K}_t$ for the Jacobian to stress that it depends on time, t.

It should be noted that we assume that both the noise terms, $\boldsymbol{\varepsilon}_t$ and $\boldsymbol{\eta}_t$, are independent of the state vector.

3.2.1 The KF update step or analysis

Under the same assumption of multivariate normal statistics as that used in Sect. 3.1, we have that the optimal KF estimate, $\hat{\boldsymbol{x}}_t$ at time t is given by (e.g. Wikle and Berliner, 2007),

$$\hat{\boldsymbol{x}}_t = \boldsymbol{x}_\mathrm{a} + \left(\mathbf{K}_t^\mathrm{T}\mathbf{S}_\varepsilon^{-1}\mathbf{K}_t + \mathbf{S}_\mathrm{a}^{-1}\right)^{-1}\mathbf{K}_t^\mathrm{T}\mathbf{S}_\varepsilon^{-1}(\boldsymbol{y}_t - \mathbf{K}_t\boldsymbol{x}_\mathrm{a}) \tag{13}$$

$$\hat{\mathbf{S}}_t = \left(\mathbf{K}_t^\mathrm{T}\mathbf{S}_\varepsilon^{-1}\mathbf{K}_t + \mathbf{S}_\mathrm{a}^{-1}\right)^{-1}$$

AMTD
6, 6873–6933, 2013

Geophysical parameters retrieval from geostationary platforms

G. Masiello et al.

We see that the optimal KF estimate for $\hat{\boldsymbol{x}}_t$ is formally equivalent to that obtained by the variational or optimal estimation approach in Sect. 3.1. We recall, once again, that in the context of *data assimilation*, $\boldsymbol{x}_\mathrm{a}$ is normally the forecast at time, t and $\mathbf{S}_\mathrm{a}$ is the error forecast covariance matrix. The estimation, $\hat{\boldsymbol{x}}_t$ is referred to as the *analysis* at time t, which has covariance matrix given by $\hat{\mathbf{S}}_t$.

One important aspect of the formal solution is that the analysis depends only on the data at time t and not on that at previous times. This property is referred to as Markov property. In fact, the formal solution for the analysis does not depend on the dynamical system directly. We can see that the expression in Eq. (13) does not contain the operator $\mathbf{H}$.

The above property is also referred to as the regularization property of KF. New data comes in at t and the KF updated state estimate is the minimizer of the quadratic form or cost function, S

$$S = \min_x \frac{1}{2}(\boldsymbol{y}_t - \mathbf{K}_t\boldsymbol{x}_t)^\mathrm{T}\mathbf{S}_\varepsilon^{-1}(\boldsymbol{y}_t - \mathbf{K}_t\boldsymbol{x}_t) + \frac{1}{2}(\boldsymbol{x}_t - \boldsymbol{x}_\mathrm{a})^\mathrm{T}\mathbf{S}_\mathrm{a}^{-1}(\boldsymbol{x}_t - \boldsymbol{x}_\mathrm{a}) \quad (14)$$

However, an important distinction with data assimilation is that $\mathbf{S}_\mathrm{a}$ is potentially generated from the process and not from an external spatial model. In fact $\mathbf{S}_\mathrm{a}$ is iterated with the process as it will become clear in examining the forecast step for the linear KF. It is important here to stress that the minimization of the form Eq. (14) needs an iterative approach because of the non linearity of the forward model and a criterion to stop iterations. We use the usual χ^2-criterion. In fact, under linearity, the value of twice the quadratic S (Eq. 14) at the minimum is distributed as a χ^2-variable with M degrees of freedom (Tarantola, 1987). A χ^2-threshold, χ^2_th at three sigma confidence interval, can be then obtained according to $\chi^2_\mathrm{th} = M + 3\sqrt{2M}$, therefore the iterative procedure is stopped when

$$\chi^2 = 2 \times S \leq \chi^2_\mathrm{th} \quad (15)$$

AMTD
6, 6873–6933, 2013

3.2.2 The KF forecast step

In our notation, $\hat{\boldsymbol{x}} = \hat{\boldsymbol{v}} - \boldsymbol{v}_{\mathrm{o}}$ and $\hat{\boldsymbol{x}}_{\mathrm{a}} = \hat{\boldsymbol{v}}_{\mathrm{a}} - \boldsymbol{v}_{\mathrm{o}}$, so that the formal KF estimate for the state vector is

$$\hat{\boldsymbol{v}}_t = \boldsymbol{v}_{\mathrm{a}} + \left(\mathbf{K}_t^{\mathrm{T}}\mathbf{S}_\varepsilon^{-1}\mathbf{K}_t + \mathbf{S}_{\mathrm{a}}^{-1}\right)^{-1}\mathbf{K}_t^{\mathrm{T}}\mathbf{S}_\varepsilon^{-1}(\boldsymbol{y}_t - \mathbf{K}_t\boldsymbol{x}_{\mathrm{a}}) \tag{16}$$

For the forecast step the KF assumes that the process evolves in a linear way, according to the operator $\mathbf{H}$, therefore we can obtain an estimate of the forecast at time $t+1$, standing at time t, through the linear transform,

$$\hat{\boldsymbol{v}}_{t+1}^{\mathrm{f}} = \mathbf{H}\hat{\boldsymbol{v}}_t \tag{17}$$

where the super-script f stands for forecast. The forecast has uncertainty given by

$$\hat{\mathbf{S}}_t^{\mathrm{f}} = \mathbf{H}\hat{\mathbf{S}}_t\mathbf{H}^{\mathrm{T}} + \mathbf{S}_\eta \tag{18}$$

where $\mathbf{S}_\eta$ is the covariance matrix of the noise term $\boldsymbol{\eta}_t$ (see Eq. 12).

As soon as new data comes in at time $t+1$, the forecast becomes the background,

$$\boldsymbol{v}_{\mathrm{a}} = \hat{\boldsymbol{v}}_{t+1}^{\mathrm{f}}, \quad \mathbf{S}_{\mathrm{a}} = \hat{\mathbf{S}}_t^{\mathrm{f}} \tag{19}$$

and we are ready to obtain the new analysis, $\hat{\boldsymbol{v}}_{t+1}$.

An important concept to draw from this sequential updating is that spatial information about the distribution of $\boldsymbol{v}_t$ can be generated from the dynamics of the process. In fact, analyzing the forecast covariance matrix Eq. (18), it is seen that it is based on the previous forecast covariance matrix and also inherits the dynamical relationship from the previous time. Thus, in the situation of assimilation for a space-time process the spatial covariance for inference is built up sequentially based on past updates with observations and propagating the posterior forward in time as a forecast distribution. We stress that this spatial information is the difference or error between the conditional mean and the true field and is not the covariance of the process itself.

AMTD
6, 6873–6933, 2013

However, the goodness of this spatial information mostly relies on the quality of the physics we model with the operator **H**. Typically, the forecast step is completed by a deterministic, physically based model. In this case, the spatial information has value. However, in case where we want the problem driven from the data, the model can be very simplistic and inherently inadequate to describe the real-world process. In this case, spatial information has to be provided externally through a proper definition of $\mathbf{S}_a$.

3.3 A formulation of the emissivity-temperature retrieval with KF

To begin with, we introduce a transform for the emissivity, which allows us to constrain the retrieval to the physical emissivity range of 0–1. Let ϵ be the emissivity at any of the channels, we consider the *logit* transform

$$e = \log \frac{\epsilon}{1-\epsilon} \tag{20}$$

which has inverse,

$$\epsilon = \frac{\exp(e)}{1+\exp(e)} \tag{21}$$

The transform maps 0–1 into the interval $[-\infty, +\infty]$ and viceversa, therefore if we work with the variable e, retrieval positiveness for ϵ is ensured.

In order to work with the parameter e we have to properly transform the Jacobian. It easily follows from Eq. (20) that

$$\frac{\partial R}{\partial e} = \frac{\partial R}{\partial \epsilon}\epsilon(1-\epsilon) \tag{22}$$

where R is the radiance at a generic channel.

If we linearize the forward model, at time t, with respect e and T_s, we obtain

$$\boldsymbol{y}_t = \mathbf{A}_t \delta \boldsymbol{e}_t + \mathbf{B}_t \delta T_{st} \tag{23}$$

AMTD
6, 6873–6933, 2013

Geophysical parameters retrieval from geostationary platforms

G. Masiello et al.

with $\delta \boldsymbol{e} = \boldsymbol{e} - \boldsymbol{e}_o$ of dimension $M \times 1$, $\delta T_{st} = T_{st} - T_{sto}$. The matrix $\mathbf{A}_t$ is the emissivity Jacobian, a diagonal matrix of size $M \times M$, and $\mathbf{B}_t$ is the surface temperature jacobian, a vector of dimension $M \times 1$. We have that the size of the observation vector, $\boldsymbol{y}_t$ is $M \times 1$, the dimension of the jacobian $\mathbf{K}_t = (\mathbf{A}_t, \mathbf{B}_t)$ is $M \times (M+1)$ and the state vector,

$$\boldsymbol{x}_t = \begin{pmatrix} \delta e_{1t} \\ \delta e_{2t} \\ \ldots \\ \delta e_{Mt} \\ \delta T_{st} \end{pmatrix} \tag{24}$$

has dimension $(M+1) \times 1$. As regards the state or model equation for emissivity, an evolution equation is straightforward if we consider the high repeat rate of SEVIRI observations (15 min), which lead us to assume that the evolution of the couple, $[T_s, \epsilon]$ has a low variability on a time scale of 1 h. This is particularly true for emissivity, but much less for temperature over land, which is strongly influenced from the daily cycle. For sea surface the assumption of a low time variability on time scales of several hours is good both for T_s and ϵ.

With this in mind, let $\boldsymbol{v} = (e_1, \ldots, e_M, T_s)^T$ be the emissivity-temperature vector, a suitable dynamical equation is then a simple persistence

$$\boldsymbol{v}_{t+1} = \mathbf{H}\boldsymbol{v}_t + \boldsymbol{\eta}_{t+1} \tag{25}$$

where, according to our notation (see Sect. 3.2), $\boldsymbol{\eta}_t$ is a noise term with covariance, $\mathbf{S}_\eta$, and $\mathbf{H}$ is the identity propagation operator.

We know that the persistence model of Eq. (25) is not physically correct since it cannot reproduce the strong daily cyclic behaviour of T_s expected in clear sky for land surface (Gottsche and Olesen, 2009; Menglin and Dickinson, 1999; Menglin, 2000). It could be a fair model for sea surface, where thermal inertia of water strongly damps the effect of the solar cycle, however it cannot represent a good model for land surface.

AMTD
6, 6873–6933, 2013

Nevertheless, it has to be stressed that within the context of the Kalman filter methodology *we do not need the exact model equation* of a given parameter (Wikle and Berliner, 2007), provided the parameters are strongly constrained by the data. To this end, an important role is played by the stochastic noise covariance, $\mathbf{S}_\eta$. In fact, it assumes a meaning and a role, which is much more important that the background covariance matrix, $\mathbf{S}_a$. This last one is used to start the iteration cycle at time, $t = 0$. At later times, the system loses its memory at a rate, which is determined by the stochastic noise term.

The stochastic term governs the asymptotic properties of the retrieval covariance, $\hat{\mathbf{S}}_t$. By properly tuning the stochastic noise covariance, we can have a retrieval which is either dominated from the data ($\mathbf{S}_\eta \rightarrow +\infty$), or the state model ($\mathbf{S}_\eta \rightarrow 0$).

SEVIRI atmospheric window channels are strongly dominated by T_s. This is exemplified in Fig. 4, which shows a simulation of the daily evolution of T_s for a desert site and the corresponding radiance signal at channels 7 (12 µm). The simulation has been obtained using the daily cycle model developed by Gottsche and Olesen (2009) on the basis of in situ real observations at a station in the Namib desert. The model fit to the data with an accuracy of ≈ 1–2 K, therefore the T_s evolution shown in Fig. 4 reflects a realistic situation.

The corresponding radiance has been obtained through σ-SEVIRI. The state vector needed for the computation of the radiance has been obtained from the ECMWF analysis for a desert site.

It is immediately seen form Fig. 4, that the radiance time-behaviour is completely dominated by the time-evolution of T_s. This is a helpful situation because, at least for temperature, we can design a Kalman filter, which is strongly driven by the data.

To this end, we first clarify how we build up $\mathbf{S}_\eta$ and $\mathbf{S}_a$ on the basis of the related matrices for emissivity and surface temperature.

AMTD
6, 6873–6933, 2013

We do not consider correlation between emissivity and surface temperature, therefore

$$\mathbf{S}_\eta = \begin{pmatrix} \mathbf{S}_{\eta e}, & \mathbf{0} \\ \mathbf{0}, & S_{\eta T_s} \end{pmatrix} \tag{26}$$

and

$$\mathbf{S}_a = \begin{pmatrix} \mathbf{S}_e, & \mathbf{0} \\ \mathbf{0}, & S_{T_s} \end{pmatrix} \tag{27}$$

where

- $\mathbf{S}_{\eta e}$ is the covariance matrix of the emissivity stochastic term
- $S_{\eta T_s}$ is the variance (scalar) of the surface-temperature stochastic term
- $\mathbf{S}_e$ is the initial background covariance matrix of the emissivity vector
- S_{T_s} is the initial background-variance (scalar) of the surface-temperature parameter

To begin with $\mathbf{S}_e$ is derived from the UW/BFEMIS data base (see Sect. 2). Its definition and calculation is time-space localized. For a given month and (lat, lon) SEVIRI pixel coordinates, UW/BFEMIS yields ten different samples of the emissivity-vector. These samples undergo the logit transform (see Eq. 20) and are used to compute the covariance matrix, $\mathbf{S}_e$.

An example of $\mathbf{S}_e$, for the set of seven SEVIRI channels (2 to 8 in Table 1), for the month of July and for a SEVIRI pixel corresponding to a site in the Sahara desert is shown in Table 2. $\mathbf{S}_e$ shown in Table 2 makes reference to the emissivity vector ordered from the long to short wave. The element (5,5) corresponds to the channel at 8.7 µm, which is in the middle of the quartz reststrhalen band and, hence, is characterized by the strongest variability.

AMTD
6, 6873–6933, 2013

The covariance matrix, $\mathbf{S}_{\eta e}$ is derived from $\mathbf{S}_{\mathrm{e}}$, considering that $\mathbf{S}_{\eta e}$ has to take correctly into account the expected variation of emissivity on a time scale comparable to the SEVIRI repeat time, which is 15 min.

This is achieved by down-scaling the covariance matrix, $\mathbf{S}_{\mathrm{e}}$ according to the procedure here illustrated. Let $S_{\mathrm{e}}(i,j); i,j = 1,\ldots,n = 7$ be the elements of $\mathbf{S}_{\mathrm{e}}$. The correlation matrix, $\mathbf{C}_{\mathrm{e}}$ is defined according to

$$C_{\mathrm{e}}(i,j) = \frac{S_{\mathrm{e}}(i,j)}{\sqrt{S_{\mathrm{e}}(i,i)S_{\mathrm{e}}(j,j)}}; \quad i,j = 1,\ldots,M = 7 \tag{28}$$

The matrix $\mathbf{S}_{\mathrm{e}}$ is scaled according to

$$S_{\mathrm{e}}^{(\mathrm{s})}(i,j) = \frac{\sqrt{S_{\mathrm{e}}(i,i)S_{\mathrm{e}}(j,j)}}{f^2} C_{\mathrm{e}}(i,j); \quad i,j = 1,\ldots,n = 7 \tag{29}$$

where $\mathbf{S}_{\mathrm{e}}^{(\mathrm{s})}$ is the matrix scaled by the factor f^2. The scaling operation above preserves the correlation structure.

We assume $\mathbf{S}_{\eta e} = \mathbf{S}_{\mathrm{e}}^{(\mathrm{s})}$. The appropriate value of f has to be tuned in simulation. After extensive simulations (Serio et al., 2013) we have that $f = 10$ is appropriate for this case study.

As far as T_{s} is concerned, based on Fig. 4, we want to stay closer to the data than the model. We have that a variance of 1 K^2 for the initial background and stochastic term, $S_{T_{\mathrm{s}}}$ and $S_{\eta T_{\mathrm{s}}}$, respectively, provides a balanced retrieval. In other words, at least for land surface, $S_{\eta T_{\mathrm{s}}}$ does not need to be down-scaled with respect to $S_{T_{\mathrm{s}}}$.

This can be seen in Fig. 5 where we show the results of a retrieval exercise obtained in simulation for the case of desert site (see Serio et al., 2013, for full details). The case shown uses a persistence model for the state equation of both emissivity and skin temperature. For emissivity this is correct, since the simulation assumes a constant emissivity at each SEVIRI channel. Conversely this is not correct for the skin temperature, whose true value follows the daily cycle shown in Fig. 5.

AMTD
6, 6873–6933, 2013

Figure 5 and the error analysis in Fig. 6 show that if we use a value of 1 K^2 for the variance of the stochastic term we correctly follow the data and retrieve the true value of the surface temperature within the accuracy determined by the a-posteriori covariance matrix.

Conversely, in the limit in which the variance of the stochastic term goes to zero (see Fig. 7), after some iterations, the retrieval just follows the persistence model. The initialization point for skin temperature in both exercises is the true temperature minus 4 °C. Note that we need to specify only the initialization point at $t = 0$, after that KF yields the retrieval on the basis of the data points and model alone.

Figures 5–7 help us to clarify that within the strategy of KF we do not need the correct physical equations governing the process, provided we can rely on data, that is observations, which strongly constrain the phenomenon under investigation. This is an important aspect of the methodology and also clarifies the key role played by the the stochastic noise term $\boldsymbol{\eta}$ and its covariance matrix, $\mathbf{S}_{\eta e}$. Failing to understand how this term works within the Kalman filter can lead to un-physical results as that, e.g., shown in Fig. 7.

Finally, we stress that for the case of sea surface a simple persistence model is accurate also for the case of skin temperature, therefore for sea surface, $S_{\eta T_s}$ needs to be down-scaled with respect to S_{T_s}. We use $S_{\eta T_s} = 1\,\mathrm{K}^2$ and a $S_{\eta T_s}$ is scaled again with a factor $f = 10$, that is $S_{\eta T_s} = 0.01\,\mathrm{K}^2$.

For the sea-surface emissivity covariance we use Masuda's model (Masuda et al., 1988). For any single SEVIRI pixel field of view angle, we generate the emissivity vector for wind speed in the range 0–15 m s^{-1} and with a step of 1.5 m s^{-1}. In this way we have 11 emissivity vectors, which are used to define background vector and covariance. Again, the resulting covariance is down-scaled by a factor $f = 10$.

The goodness of the persistence model for sea surface has been checked directly on the basis of real observations, because for sea surface the ECMWF analysis is credited of an accuracy within ±1 K. Figure 8 exhibits the results for the sea target area

AMTD
6, 6873–6933, 2013

Geophysical parameters retrieval from geostationary platforms

G. Masiello et al.

shown in Fig. 2 and for 31 July 2010. From Fig. 8 we see that a stochastic variance term below 0.25 K^2 tends to have a better agreement with the ECMWF model, which leads us to conclude that for sea surface a persistence model is effective also for T_s and not only for emissivity.

In passing, we also note from Fig. 8 that the skin temperature reaches a maximum around 3 p.m. LT, whereas ECMWF indicates a maximum near noon. The maximum around 3 p.m. is in agreement with Gentemann et al. (2003), who shows that during the daytime, solar heating may lead to the formation of a near-surface diurnal warm layer, particularly in regions with low wind speeds. Analysis of TMI (Tropical Rainfall Measuring Mission's (TRMM) Microwave Imager) and AVHRR skin temperature have revealed that the onset of warming begins as early as 8 a.m. and peaks near 3 p.m., with a magnitude of 2.8 °C during favorable conditions.

3.4 Sensitivity to the atmospheric state vector

For the problem of $[T_s, \epsilon]$ retrieval we consider SEVIRI atmospheric window channels alone, namely channels 4, 6 and 7 (see Table 1). However, in principle also atmospheric window channels can have contribution from atmospheric parameters ($[T, Q, O]$), which give the major emission contribution between 8–12 µm.

In the present scheme, the retrieved state vector includes $[T_s, \epsilon]$ alone, whereas the principal atmospheric parameters are obtained by the ECMWF analysis. Thus, the problem arises about the potential bias on the retrieved parameters $[T_s, \epsilon]$, which could come from the uncertainty of those not-retrieved, that is $[T, Q, O]$.

We stress that in our scheme the (non-retrieved) atmospheric state vector, $[T, Q, O]$ is obtained from the time-space collocated ECMWF analysis, which, especially for arid regions, such as that analyzed in this paper, can be significantly in error in daytime (Masiello and Serio, 2013).

The assessment of the potential bias on the retrieved couple $[T_s, \epsilon]$, which can arise form a non perfect knowledge of the atmospheric state vector can be performed

AMTD
6, 6873–6933, 2013

through a linear perturbation analysis by dealing with a generic atmospheric parameter, say $\mathbf{X}$ as a interfering factor.

Within the context of optimal estimation, e.g., Rodgers (2000), which (as shown in Sect. 3.2.1) applies to any iteration step of the Kalman filter methodology, the sensitivity of the retrieved vector, $\hat{\boldsymbol{v}}$ to a difference $\Delta\mathbf{X} = \mathbf{X} - \mathbf{X}_\mathrm{o}$ of the given atmospheric parameter, $\mathbf{X}$ with respect to the reference state, $\mathbf{X}_\mathrm{o}$ assumed in the forward model calculations, can be computed according to (Carissimo et al., 2005)

$$\Delta\hat{\boldsymbol{v}} = \left(\mathbf{K}^\mathrm{T}\mathbf{S}_\varepsilon^{-1}\mathbf{K} + \mathbf{S}_\mathrm{a}^{-1}\right)^{-1}\mathbf{K}^\mathrm{T}\mathbf{S}_\varepsilon^{-1}\mathbf{K}_X\Delta\mathbf{X} \tag{30}$$

where $\mathbf{K}$ is the Jacobian matrix of the retrieved vector and $\mathbf{K}_X$ is the Jacobian matrix of the interfering factor computed at the reference state, $\mathbf{X}_\mathrm{o}$.

Equation (30) can be used to check the impact of possible biases in the ECMWF analysis on the retrieval for surface emissivity and temperature. To consider a realistic situation, we have used a couple of day–night IASI spectra (see Fig. 9) recorded on 10 July 2010 over the Sahara desert at two close locations which are included in the target area shown in Fig. 2. These two IASI spectra have been inverted for $[T_\mathrm{s}, \epsilon, T, Q, O]$ using the so-called φ-IASI package (Amato et al., 1995; Masiello and Serio, 2004; Carissimo et al., 2005; Grieco et al., 2007; Masiello et al., 2009; Masiello and Serio, 2013). The IASI retrieved atmospheric state vector is compared to the ECMWF reference state vector in Fig. 9. From this figure, we see that large differences arise in daytime, which concern mostly the lower troposphere. For nighttime we have a good agreement also for the surface temperature (303.9 K of ECMWF vs 303 K of IASI), whereas for daytime we have a disagreement, which is as large as 12 K (310.1 of ECMWF vs 321.7 of IASI).

We can take the difference, $\mathbf{X}_\mathrm{IASI} - \mathbf{X}_\mathrm{ECMWF}$ as a realistic departure of the ECMWF analysis from the *true* atmospheric state vector and compute, through Eq. (30), the resulting bias over the retrieved surface emissivity and temperature. In doing so, we

AMTD
6, 6873–6933, 2013

have used for $\mathbf{S}_a$ defined according to

$$\mathbf{S}_a = \begin{pmatrix} \mathbf{S}_e, & \mathbf{0} \\ \mathbf{0}, & 1\,\mathrm{K}^2 \end{pmatrix} \tag{31}$$

with $\mathbf{S}_e$ obtained by the UW/BFEMIS data base. It should be stressed that $\mathbf{S}_a$ defined in Eq. (31) gives the less favorable situation. In fact, as iterations evolve, the matrix, $\mathbf{S}_a$ evolves as well according to Eq. (18) and its norm tends to decrease. In this situation, it can be shown (Carissimo et al., 2005) that the interfering effect tend to decrease, as well. Thus the calculations we are going to show have to be considered as a sort of upper boundary to the impact of interfering atmospheric factors.

With this in mind, Table 3 shows the impact over the retrieval of the interfering factors, $[T, Q, O]$. It is seen that also in the less favorable case, the impact is modest and much lower than the precision of the retrieval. As expected, the impact is larger during daytime, although normally affecting the second decimal digit for skin temperature and below the fourth decimal digit for emissivity.

Based on this result, we have implemented the $[T_s, \epsilon]$-version of the Kalman filter methodology by considering the simultaneous uses of channels 4, 6 and 7 and neglecting the possible contribution to Eq. (23) from the atmospheric parameters, if not that considered through the ECMWF reference state.

Finally, as evidenced in this section the impact of possible interfering factors depends on the regularization scheme, that is the matrix $\mathbf{S}_a$ and tends to attain its largest value in the limit $\mathbf{S}_a \rightarrow 0$ (Carissimo et al., 2005), that is for the case of unconstrained least squares.

AMTD
6, 6873–6933, 2013

4 Results

4.1 Assessing the performance of the emissivity-temperature retrieval

We begin with the description of results obtained by processing SEVIRI data at the three small test area shown in Fig. 2. With this first series or results we want to address issues such as the precision of the method and its convergence properties. Results obtained form the analysis of the full target area will be shown later in this section.

The Kalman filter has been applied to SEVIRI atmospheric channels alone. These are the channels at 12, 10.8 and 8.7 µm. The corresponding channel emissivity and the surface temperature have been simultaneously retrieved with a time resolution of 15 min.

For the sake of clearness, Table 4 summarizes the many settings of the filter. Note that in computing background vector and related covariance matrix from the UW/BFEMIS data base we have not used the data for July 2010, which are used for comparison with our results.

Figure 10 allows us to exemplify the precision of the methodology. The retrieval has been obtained for one single day, one single SEVIRI pixel from the Sahara desert test area and therefore corresponds to the highest time-space resolution of the methodology. It is possible to see that even for a time resolution of 15 min, temperature is obtained with a precision of $\approx \pm 0.2$ K and better, whereas emissivity is obtained with a precision better than $\approx \pm 0.005$. The emissivity retrieval shown in Fig. 10 correspond to the channel at 8.7 µm. This channel is the in middle of the quartz reststrhalen band and has the higher contrast in the atmospheric window. From Fig. 10, we see that the emissivity tends to follow the daily cycle, with lower values obtained during night-time/early morning.

This is better evidenced from the analysis of the the long sequence of clear sky days shown in Figs. 11 and 12. The analysis refers to a single SEVIRI pixel in the Sahara desert (30.66° N, 5.56° E) and has been performed with a time resolution of 15 min. According to Li et al. (2012), we have that the amplitude of the daily cycle is quite

AMTD
6, 6873–6933, 2013

evident for the SEVIRI channel at 8.7 µm where peak-to-peak variations can reach ≈ 0.03. Smaller variations are found at 10.8 µm (below 0.01). At 12 µm the variation is much less pronounced and in some cases it seems to have a reverse sign with respect to the pattern at 8.7 µm, an effect which has been reported also by Li et al. (2012).

These daily variation of emissivity over desert sand, even in the dry (non-raining) season, have been first reported by Li et al. (2012). It is very likely that these variations are the result of day–night sand evotranspiration, which occurs for direct adsorption of water vapour at the surface (Agam and Berliner, 2004, 2006; Mira et al., 2007). Clear sky daily variation of emissivity is more pronounced for desert sand because of the strong contrast of quartz absorption band at 8.6 µm.

However, it should be noted that the a-posteriori covariance matrix of the analysis, $\hat{\mathbf{S}}_t$ (see Eq. 13) shows a relatively strong anti-correlation of the retrieved T_s vs ϵ. This anti-correlation can be as large as −0.5. It is a result of the data equation (that is the radiative transfer equation). It cannot depend on the evolution equation, because the stochastic covariance matrix is block diagonal (see Eq. 27). This anti-correlation could introduce some systematic drift in the retrieved parameters, and therefore could potentially be a spurious cause of the diurnal variation seen in emissivity.

Nevertheless, based on our present retrieval exercises with real and simulated observations, it seems that a constant emissivity is not capable of introducing a cyclic behaviour in the retrieval (as an example, see the simulation provided in Figs. 5 and 6). Moreover, for non arid-lands we have observed situations in which the day–night emissivity variation, despite the anticorrelation $T_\mathrm{s} - \epsilon$, is in phase with the daily temperature cycle (e.g. see Sect. 4.2), that is the reverse situation we have observed for condition over desert sand. Furthermore, IASI observations (Masiello et al., 2013) confirm that the daily variation of emissivity is a genuine feature in the data. Finally, Hulley et al. (2010) has shown that emissivity retrieval from satellite observations is sensitive to changes in soil moisture.

Figures 10–12 are meant to exemplify that our physical scheme is sensitive to these day–night emissivity variations. An in depth assessment of this effect is ongoing. As

AMTD
6, 6873–6933, 2013

already stressed in Sect. 1, the present study mostly focuses on the novel aspect of the methodology and comparison of its results with in situ data, and other similar satellite products.

Bearing this in mind, we go back to Fig. 11 from which it is possible to see that a slight cloudiness affects the observations at the beginning of the second day. We do not skip these observations when performing the retrieval, therefore Fig. 11 shows that slight cloudiness does not bring the Kalman filter to an unstable region. In other words, the stability of the filter is not influenced by slight cloudiness, although this information is forward propagated through the forecast.

However, overcast conditions that persist a long time (e.g. from t_1 to t_2, with $t_2 - t_1 \gg 15$ min) can (e.g. because of rain) drastically change the emissivity at the endpoints t_1 and t_2. Furthermore, cloudy radiances could be undetected, in which case serious overcast conditions could negatively influence the retrieval products. To avoid this effect, cloudy radiances (if detected) are just skipped within the KF scheme and, furthermore, only retrieval which satisfies the cost function condition of Eq. (15) are propagated through the filter. To this end, it should be stressed that KF does not need to deal with equally spaced times.

This is exemplified in Fig. 13, which shows the retrieval for surface temperature corresponding to whole month of July for the Seville test area. The analysis has been performed only for clear sky soundings (according to the operational SEVIRI cloud mask) and has been spatially averaged over the 187 available SEVIRI pixels. Cloudy radiances are skipped in the analysis, which means that we use a time step which is not a constant. Missing values of the surface temperature in Fig. 13 correspond to cloudy radiances. However, undetected cloudy observations could be also processed, which can drift the filter to regions which do not correspond to the cost function below the prescribed χ^2-threshold. Therefore, retrievals are only considered and propagated ahead only in case the cost function $\chi^2 = 2S$ has been reduced below the χ^2-threshold. These *good* retrievals are shown in Fig. 13.

AMTD
6, 6873–6933, 2013

The retrieval for emissivity is shown again in Fig. 13 (bottom panel). Also in this case, the results have been averaged over spatially adjacent clear sky pixels. We stress that clear sky is defined according to the SEVIRI cloud mask, which can still contain undetected cloudiness. These undetected clouds cause the occasional spikes seen in Fig. 13. It is also interesting to note, that also for Seville we see a cyclic emissivity behaviour, although now the amplitude of these variations is confined within ±0.01.

Figure 14 exemplifies the analysis for the case of sea surface. The retrieval for $T_s - \epsilon$ refers to the Mediterranean target area shown in Fig. 2. Also in this case the results have been spatially averaged. Possible gaps in the time sequence correspond to time intervals characterized by the presence of cloudiness.

4.2 Comparison with ECMWF T_s, AVHRR-AMSR and in situ land surface temperature observations

Figure 11 shows that the ECMWF model compares fairly well with the retrieval at night-time hours, whereas during daytime ECMWF surface temperature is biased significantly low. This is in line with the deficiencies in ECMWF model skin temperature identified by Trigo and Viterbo (2003).

To have a better assessment of this bias, we have spatially averaged the data over the ECMWF grid box of $0.5^\circ \times 0.5^\circ$. In this way the results are much more consistent with the horizontal spatial resolution of the ECMWF analysis.

The results are shown in Fig. 15. For the desert site, we have that the bias at midday reaches about 9 °C and has a minimum at midnight, when the bias is about 1 °C. At 06:00 and 18:00 UTC the bias is still negative and has a magnitude of about 2 °C.

For the case of the test site of Seville, we have observed a negative bias of ≈ 7 °C at midday. However, for the other three canonical hours of the ECMWF analysis, the bias is below 1 °C.

A much better comparison has been obtained in the case of the ocean site, also shown in Fig. 15. In this case, the overall bias is about −0.3 °C (ECMWF is slightly warmer than KF). However, we also see a dependence with the hour of the day. The bias is almost zero at 00:00 and 18:00 UTC, and reaches $\approx -0.6\,^{\circ}$C at 12:00 UTC. Thus, also for sea surface it seems that the ECMWF model has a bias, which depends on the daily cycle.

A very nice agreement has also been found with the AMSR+AVHRR OISST analysis (see Fig. 16). The analysis has been used to compute the skin temperature over the small Mediterranean target area shown in Fig. 2. The results show that SEVIRI KF captures the correct day-to-day variations of the skin temperature. Daily average temperatures agree within 0.5 °C, whereas the agreement of the monthly average temperature is within 0.1 °C (23.93 °C SEVIRI KF vs 24.06 °C of AMSR+AVHRR OISST). The relatively large difference (about 0.7 °C) around days 23–24 is likely due to the effect of cloudiness combined to the coarser spatial resolution of the OISST analysis.

Finally, we will now show and discuss the comparison with in situ land surface temperature observations at Evora station (Southern Portugal). For this station the SEVIRI KF analysis for temperature and emissivity was computed for all clear observations, with clear sky defined according to the SEVIRI operational cloud mask.

Figure 17 (upper panel) compares the surface temperature for three consecutive clear sky days in July 2010. It is seen that the SEVIRI KF analysis is slightly upward biased with respect to the in situ observations both at midday and before sunrise. This behaviour is also obtained for the LSA SAF T_s product and can be partially explained by the heterogenous scene, even though the methodology used to process in situ observations try to minimize this effect. When we consider the comparison with SEVIRI LSA SAF product, the midday and night-time bias tend to be confined well below 1 °C. The position of Meteosat-9 with respect to Evora, favours the observation of sunlit surfaces. The current compositing of ground data does not include an accurate weighing of sunlit and shadowed ground fractions, which also may lead to in situ temperatures being cooler than those actually observed by SEVIRI. This is further corroborated by the comparison between SEVIRI KF analysis for temperature, and the SEVIRI LSA SAF T_s product: two independent methodologies produce very close values, with negligible systematic differences and standard deviation of about 0.8 °C.

AMTD
6, 6873–6933, 2013

Emissivity retrieval for Evora (see Fig. 17), with the highest value obtained for 8.7 µm, clearly above that obtained for 10.8 µm, is consistent with the emissivity spectra for dry grass (Seemann et al., 2008; Baldridge et al., 2009). This is in agreement with the type of landscape observed around the station during the summer, when the understory dries out completely.

Also for Evora an emissivity wavy pattern is visible, although its amplitude is very small (it is within ±0.005, as exemplified in Fig. 17 (bottom panel)). LSA SAF analysis uses an almost constant emissivity at 10.8 µm, which has a value of 0.975 (black line in Fig. 17). The SEVIRI KF analysis shows that the emissivity at this channel is ≈ 0.972 and varies in phase with the daily temperature cycle. Although, as said the amplitude of this variation is of the order of few parts per thousand.

The full set of SEVIRI KF temperature retrieval for the Evora station is compared to in situ observations in the scatter plot of Fig. 18. This figure confirms the presence of a positive bias of 1.10 °C in the KF analysis. Again, we stress that this difference is within the uncertainty of the comparison between in situ and satellite observations. The bias is nearly zero, when we compare SEVIRI KF to SEVIRI LSA SAF.

4.3 Monthly maps

Finally, we have used the scheme to perform $[T_s, \epsilon]$ retrieval over the full target area for land surface.

Figure 19 shows the monthly map for the surface temperature and compares it with the equivalent map derived from the ECMWF analysis. The comparison allows us to appreciate the high horizontal spatial resolution (0.05° × 0.05°) compared to that of ECMWF which is ten times less resolved (0.5° × 0.5°). Because of the monthly average, differences tend to be lower than those seen for hourly and daily values. However, especially for the arid regions differences up to 5 K are still visible.

Figure 20 shows the monthly map of the channel emissivity at 8.7 µm. The difference with the UW/BFEMIS data base for the same month and geographic region is also shown in the same figure. Differences appears to be more marked for the desert

AMTD
6, 6873–6933, 2013

sand, where the variability is much larger because of the strong response from quartz particles. However, the agreement is generally good and no important deviations are seen. The map of the channel emissivity at 8.7 µm shows very well the details of seas of sand in the Sahara desert. These correspond to the most bluish part in the map and are characterized by the lower value of emissivity.

For the other two window channels, the corresponding maps are not shown for the sake of brevity. The comparison of the results with monthly maps from the UW/BFEMIS data base for the same date and location shows that differences for these channels are normally below 0.01 (Serio et al., 2013).

5 Conclusions

In this paper we have described a Kalman filter methodology and its implementation for the retrieval of surface temperature and emissivity from SEVIRI atmospheric window infrared channels.

The methodology has been applied to a case study characterized by many surface features (vegetation, cultivation, urban areas, bare soil, desert sand and sea water, to name a few).

It has been shown that by properly tuning the parameters of the state equation, we can properly model the two different time scales of emissivity and temperature and, hence, develop a method which allows us to separate emissivity from temperature within the observation equation (that is the radiative transfer equation).

The analysis performed on the basis of a case study has allowed us to reveal a lot of important features regarding the time evolution of emissivity. For desert sand we observe day–night variations, which are anti-correlated with the daily temperature cycle. Conversely, for other types of surface features, it seems that there is a very slight day–night variation, which tends to follow the daily temperature cycle.

It has been shown that the Kalman filter can handle unevenly space data acquisition times, which allows us to process long sequences of data in which cloudy observations

AMTD
6, 6873–6933, 2013

are simply skipped. However, the effect of raining clouds can alter the emissivity and introduce sharp gradients in its time evolution, which could be even in contrast with the persistence state equation and the relative large time scale assumed for this parameter. This effect could be alleviated by re-initializing the Kalman filter in presence of a big gap in the time sequence because of cloudiness. However, this is a point that has to be addressed with suitable case studies and, therefore, needs further investigation.

The results have been compared to several independent observations. These comparisons lead us to conclude that the scheme is accurate and can be reliably extended to the full disk.

Finally, we want to stress that, although the case study developed in this study is necessarily limited to surface parameters, because of limited information content of SEVIRI infrared channels as far as atmospheric parameters are concerned, the retrieval methodology has been described in its most general framework and can, therefore, provide guidelines to extend the algorithms to future instruments, such as MTG-IRS. This instrument will have some 2000 spectral channels. Therefore, the data space, rather than the parameter space, will be driving the design of a L2 processor. Even with $M = 2000$ a 2-D Kalman filter (time × vertical) is feasible in terms of computational costs. In this respect, if we consider that the observational covariance matrix for MTG-IRS is expected to be nearly diagonal (which implies conditional independence of the observations), the Kalman filter update can be done sequentially (Nychka and Anderson, 2010; Rodgers, 2000). With this approach we need to store only $M = 2000$ diagonal elements and use a numerical algorithm which does not involve any matrix inversion. From a computational point of view, the dimensionality of the problem would be driven by the analysis covariance matrix, $\mathbf{S}_a$, which at this point could include also suitable spatial constraints, which could make the methodology, 4-D. However, in case we consider to use, e.g., the ECMWF analysis or forecast directly as the state equation of the Kalman filter, we could avoid to include spatial constraints and rely on the spatial homogeneity expected in the ECMWF analysis or forecast.

AMTD
6, 6873–6933, 2013

Acknowledgements. IASI has been developed and built under the responsibility of the Centre National d'Etudes Spatiales (CNES, France). It is flown onboard the Metop satellites as part of the EUMETSAT Polar System. The IASI L1 data are received through the EUMETCast near real time data distribution service. Work partially supported through EUMETSAT contract EUM/CO/11/4600000996/PDW and project Ritmare-Ricerca Italiana per il Mare (CNR-MIUR). The ground data gathered at Evora were kindly provided by Frank Goettsche (KIT), member of the EUMETSAT LSA SAF Team.

References

Agam, N. and Berliner, P. R.: Diurnal water content changes in the bare soil of a coastal desert, J. Hydrometeorol., 5, 922–933, doi:10.1175/1525-7541(2004)005<0922:DWCCIT>2.0.CO;2, 2004. 6898

Agam, N. and Berliner, P. R.: Dew formation and water vapor adsorption in semi-arid environments: a review, J. Arid Environ., 65, 572–590, doi:10.1016/j.jaridenv.2005.09.004, 2006. 6898

Amato, U., Carfora, M. F., Cuomo, V., and Serio, C.: Objective algorithms for the aerosol problem, Appl. Optics, 34, 5442–5452, doi:10.1364/AO.34.005442, 1995. 6895

Amato, U., Masiello, G., Serio, C., and Viggiano, M.: The σ-IASI code for the calculation of infrared atmospheric radiance and its derivatives, Environ. Modell. Softw., 17, 651–667, 2002. 6880, 6881

Baldridge, A. M., Hook, S. J., Grove, C. I., and Rivera, G.: The ASTER spectral library version 2.0, Remote Sens. Environ., 113, 711–715, doi:10.1016/j.rse.2008.11.007, 2009. 6902

Borbas, E. E. and Ruston, B. C.: The RTTOV UWiremis IR land surface emissivity module, NWP SAF, EUMETSAT, Darmstadt, Germany, 2010. 6879

Carissimo, A., De Feis, I., and Serio, C.: The physical retrieval methodology for IASI: the δ-IASI code, Environ. Modell. Softw., 20, 1111–1126, doi:10.1016/j.envsoft.2004.07.003, 2005. 6883, 6895, 6896

Clough, S. A., Shephard, M. W., Mlawer, E. J, Delamere, J. S., Iacono, M. J., Cady-Pereira, K., Boukabara, S., and Brown, P. D.: Atmospheric radiative transfer modeling: a summary of the AER codes, J. Quant. Spectrosc. Ra., 91, 233–244, 2005. 6881

Courtier, P.: Variational methods, J. Meteorol. Soc. Jpn., 75, 211–218, 1997. 6883

AMTD
6, 6873–6933, 2013

Cuomo, V., Serio, C., Crisciani, F., and, Ferraro, A.: Discriminating randomness from chaos with application to a weather time series, Tellus A, 46, 299–313, doi:10.1034/j.1600-0870.1994.t01-2-00005.x, 1994. 6875

Dash, P., Olesen, F. S., and Prata, A. J.: Optimal land surface temperature validation site in Europe for MSG, in: Proceedings of EUMETSAT Meteorological Satellite Conference, Prague, 31 May–4 June 2004, EUMP, 41, 2004. 6880

Freitas, S. C., Trigo, I. F., Bioucas-Dias, J. M., and Gottsche, F.-M.: Quantifying the uncertainty of land surface temperature retrievals from SEVIRI/Meteosat, IEEE T. Geosci. Remote, 48/1, 523–534, doi:10.1109/TGRS.2009.2027697, 2010. 6880

Gentemann, C. L., Donlon, C. J., Stuart-Menteth, A., and Wentz, F. J.: Diurnal signals in satellite sea surface temperature measurements, Geophys. Res. Lett., 30, 1140, doi:10.1029/2002GL016291, 2003. 6894

Gottsche, F. and Olesen, F.: A simple physically based model of diurnal cycles of land surface temperature, in: Proceedings of EUMETSAT Meteorological Satellite Conference Bath, UK, 21–25 September 2009, EUMP.55, S4-20, 2009. 6889, 6890

Grieco, G., Masiello, G., Matricardi, M., Serio, C., Summa, D., and Cuomo, V.: Demonstration and validation of the φ-IASI inversion scheme with NAST-I data, Q. J. Roy. Meteorol. Soc., 133, 217–232, doi:10.1002/qj.162, 2007. 6895

Hilton, F., Armante, R., August, T., Barnet, C., Bouchard, A., Camy-Peyret, C., Capelle, V., Clarisse, L., Clerbaux, C., Coheur, P. F., Collard, A., Crevoisier, C., Dufour, G., Edwards, D., Faijan, F., Fourrié, N., Gambacorta, A., Goldberg, M., Guidard, V., Hurtmans, D., Illingworth, S., Jacquinet-Husson, N., Kerzenmacher, T., Klaes, D., Lavanant, L., Masiello, G., Matricardi, M., McNally, A., Newman, S., Pavelin, E., Payan, S., Péquignot, E., Peyridieu, S., Phulpin, T., Remedios, J., Schlüssel, P., Serio, C., Strow, L., Stubenrauch, C., Taylor, J., Tobin, D., Wolf, W., and Zhou, D.: Hyperspectral earth observation from IASI: four years of accomplishments, B. Am. Meteorol. Soc., 93, 347–370, doi:10.1175/BAMS-D-11-00027.1, 2012. 6878

Hulley, G. C., Hook, S. J., and Baldridge, A. M.: Investigating the effects of soil moisture on thermal infrared land surface temperature and emissivity using satellite retrievals and laboratory measurements, Remote Sens. Environ., 114, 1480–1493, doi:10.1016/j.rse.2010.02.002, 2010. 6898

AMTD
6, 6873–6933, 2013

Geophysical parameters retrieval from geostationary platforms

G. Masiello et al.

Kabsch, E., Olesen, F. S., and Prata, A.: Initial results of the land surface temperature (LST) validation with the Evora, Portugal, ground-truth station measurements, Int. J. Remote Sens., 29, 5329–5345, doi:10.1080/01431160802036326, 2008. 6880

Kalman, R. E.: A new approach to linear filtering and prediction problems, J. Basic Eng.-T. ASME, 82, 35–45, 1960. 6875, 6884

Kalman, R. E. and Bucy, R. S.: New results in linear filtering and prediction theory, J. Basic Eng.-T. ASME, 83, 95–107, 1961. 6875, 6884

Li, J., Li, Z., Jin, X., Schmit, T. J., Zhou, L., and Goldberg, M.: Land surface emissivity from high temporal resolution geostationary infrared imager radiances: 1. Methodology and simulation studies, J. Geophys. Res., 116, D01304, doi:10.1029/2010JD014637, 2011. 6876

Li, Z., Li, J., Li, Y., Zhang, Y., Schmit, T. J., Zhou, L., Goldberg, M. D., and Menzel, W. P.: Determining diurnal variations of land surface emissivity from geostationary satellites, J. Geophys. Res., 117, D23302, doi:10.1029/2012JD018279, 2012. 6897, 6898

Li, Z.-L., Tang, B.-H., Wu, H., Ren, H., Yan, G., Wan, Z., Isabel, F. Trigo, I. F., and Sobrino, J. A.: Satellite-derived land surface temperature: current status and perspectives, Remote Sens. Environ., 131, 14–37, doi:10.1016/j.rse.2012.12.008, 2013. 6876

Masiello, G. and Serio, C.: An effective water vapor self-broadening scheme for look-up-table-based radiative transfer, SPIE – The International Society for Optical Engineering, 4882, 52–61, 2003. 6881

Masiello, G. and Serio, C.: Dimensionality-reduction approach to the thermal radiative transfer equation inverse problem, Geophys. Res. Lett., 31, L11105, doi:10.1029/2004GL019845, 2004. 6895

Masiello, G. and Serio, C.: Simultaneous physical retrieval of surface emissivity spectrum and atmospheric parameters from infrared atmospheric sounder interferometer spectral radiances, Appl. Optics, 52, 2428–2446, doi:10.1364/AO.52.002428, 2013. 6876, 6880, 6894, 6895

Masiello, G., Serio, C., Carissimo, A., Grieco, G., and Matricardi, M.: Application of σ-IASI to IASI: retrieval products evaluation and radiative transfer consistency, Atmos. Chem. Phys., 9, 8771–8783, doi:10.5194/acp-9-8771-2009, 2009. 6895

Masiello, G., Serio, C., and Antonelli, P.: Inversion for atmospheric thermodynamical parameters of IASI data in the principal components space, Q. J. Roy. Meteorol. Soc., 138/662, 103–117, doi:10.1002/qj.909, 2011.

Masiello, C., Serio, C., Venafra, S., De Feis, I., and Borbas, E. E.: Day-night variation of Sahara desert sand emissivity during the dry season from IASI observations, J. Geophys. Res., submitted, 2013. 6879, 6898

Masuda, K., Takashima, T., and Takayama, Y.: Emissivity of pure and sea waters for the model sea surface in the infrared window regions, Remote Sens. Environ., 24, 313–329, 1988. 6893

Menglin, J.: Interpolation of surface radiative temperature measured from polar orbiting satellites to a diurnal cycle: 2. Cloudy-pixel treatment, J. Geophys. Res., 105, 4061–4076, 2000. 6889

Menglin, J. and Dickinson, R. E.: Interpolation of surface radiative temperature measured from polar orbiting satellites to a diurnal cycle: 1. Without clouds, J. Geophys. Res., 104, 2105–2116, 1999. 6889

Mira, M., Valor, E., Boluda, R., Caselles, V., and Coll, C.: Influence of soil water content on the thermal infrared emissivity of bare soils: implication for land surface temperature determination, J. Geophys. Res., 112, F04003, doi:10.1029/2007JF000749, 2007. 6898

Nychka, D. W. and Anderson, J. L.: Data assimilation, in: Handbook of Spatial Statistics, edited by: Gelfand, A., Diggle, P., Guttorp, P., and Fuentes, M., Chapman & Hall/CRC, Boca raton, FL, USA 477–494, 2010. 6875, 6876, 6904

Rodgers, C. D.: Inverse methods for atmospheric sounding, in: Theory and Practice, World Scientific, Singapore, 256 pp., 2000. 6876, 6882, 6884, 6895, 6904

Seemann, S. W., Borbas, E. E., Knuteson, R. O., Stephenson, G. R., and Huang, H. L.: Development of a global infrared land surface emissivity database for application to clear sky sounding retrievals from multispectral satellite radiance measurements, J. Appl. Meteorol. Climatol., 47, 108–123, doi:10.1175/2007JAMC1590.1, 2008. 6879, 6902

Serio, C.: Discriminating low-dimensional chaos from randomness: a parametric time series modelling approach, Il Nuovo Cimento, 107, 681–702, 1992. 6875

Serio, C.: Autoregressive representation of time series as a tool to diagnose the presence of chaos, Europhys. Lett., 27, 103, doi:10.1209/0295-5075/27/2/005, 1994. 6875

Serio, C., Masiello, G., Amoroso, M., Venafra, S., Amato, U., and De Feis, I.: Study on space-time constrained parameter estimation from geostationary data, Final Progress Report, EUMETSAT contract No. EUM/CO/11/4600000996/PDW, Darmstadt Germany, 2013. 6879, 6892, 6903

Talagrand, O.: Assimilation of observations, an introduction, J. Meteorol. Soc. Jpn, 75, 191–209, 1997. 6883

Tarantola, A.: Inverse Problem Theory: Methods for Data Fitting and Model Parameter Estimation, Elsevier, New York, 1987. 6883, 6884, 6886

Trigo, I. F. and Viterbo, P.: Clear sky window channel radiances: a comparison between observations and the ECMWF model, J. Appl. Meteorol., 42, 1463–1479, 2003. 6900

Trigo, I. F., Monteiro, I. T., Olesen, F., and Kabsch, E.: An assessment of remotely sensed land surface temperature, J. Geophys. Res., 113, D17108, doi:10.1029/2008JD010035, 2008. 6880

Wikle, C. K. and Berliner, L. M.: A bayesian tutorial for data assimilation, Physica D, 230, 1–26, doi:10.1016/j.physd.2006.09.017, 2007. 6882, 6884, 6885, 6890

Wikle, C. K. and Hooten, M. B.: A general science-based framework for dynamical spatio-temporal models, Test, 19, 417–451, doi:10.1007/s11749-010-0209-z, 2010.

AMTD

6, 6873–6933, 2013

Geophysical parameters retrieval from geostationary platforms

G. Masiello et al.

Table 1. Definition of SEVIRI infrared channels and radiometric noise in Noise Equivalent Difference Temperature (NEDT) at a scene temperature of 280 K.

Channel Number	wave number (cm^{-1})	wavelength (µm)	NEDT at 280 K (K)
1	2564.10	3.9	
2	1612.90	6.2	0.12
3	1369.90	7.3	0.20
4	1149.40	8.7	0.13
5	1030.9	9.7	0.21
6	925.90	10.8	0.13
7	833.30	12.0	0.18
8	746.30	13.4	0.37

AMTD
6, 6873–6933, 2013

Table 2. Example of the matrix $\mathbf{S}_e$ for a SEVIRI pixel corresponding to a desert site (30.66° N, 5.56° E). The covariance matrix has been computed for the SEVIRI channels 2 to 8 in Table 1 and makes reference to the emissivity vector ordered from the long to short wave. The element (5,5) corresponds to the channel at 8.7 µm, which is in the middle of the quartz reststrhalen band and, hence, is characterized by the strongest variability.

Row	Column						
	1	2	3	4	5	6	7
1	0.0273	0.0265	0.0136	0.0070,	0.0109	−0.0025	0.0053
2	0.0265	0.0262	0.0137	0.0068	0.0100	−0.0025	0.0057
3	0.0136	0.0137	0.0075	0.0037	0.0056	−0.0017	0.0032
4	0.0070	0.0068	0.0037	0.0023	0.0028,	−0.0008	0.0012
5	0.0109	0.0100	0.0056	0.0028	0.0067	−0.0018	0.0018
6	−0.0025	−0.0025	−0.0017	−0.0008	−0.0018	0.0008	−0.0007
7	0.0053	0.0057	0.0032	0.0012	0.0018	−0.0007	0.0017

AMTD
6, 6873–6933, 2013

Table 3. Potential bias affecting the retrieval of surface emissivity and temperature due to atmospheric parameters. The bias is dimensionless for emissivity and in K for the surface temperature.

Retrieved parameter	Interfering atmospheric parameter		
	Temp. profile	H_2O profile	Ozone profile
Day			
Emissivity at 12 µm	0.0000	0.0000	0.0000
Emissivity at 10.8 µm	0.0000	0.0000	0.0000
Emissivity at 8.7 µm	0.0000	0.0001	0.0000
Surface temperature	0.0013	0.0021	0.0004
Night			
Emissivity at 12 µm	0.0000	0.0000	0.0000
Emissivity at 10.8 µm	0.0000	0.0000	0.0000
Emissivity at 8.7 µm	0.0000	−0.0001	0.0000
Surface temperature	0.0014	−0.0014	0.0003

AMTD
6, 6873–6933, 2013

Table 4. Summary of the settings for the KF scheme.

Element	Setting/Reference
Emissivity model equation	Persistence
surface Temp. model equation	Persistence
Emissivity true values	unknown
Emissivity initial background vector (at time = 0)	average from UW/BFEMIS data base, over the years 2003–2012, but 2010
Emissivity initial background $\mathbf{S}_e$ (at time = 0)	from UW/BFEMIS data base, 2003–2012, but 2010
Emissivity stochastic covariance, $\mathbf{S}_{\eta e}$	as line above scaled down with $f = 10$
surface Temp. true values	unknown
surface Temp. initial value (at time = 0)	ECMWF analysis at 00:00 UTC
surface Temp. initial background, S_{T_s}	$1\,K^2$
surface Temp. stochastic variance $S_{\eta T_s}$	as S_{T_s} for land, S_{T_s}/f^2, with $f = 10$ for sea surface
Observational Covariance matrix, $\mathbf{S}_\varepsilon$	diagonal, from SEVIRI radiometric noise
Atmospheric profiles	assumed known, time-space colocated ECMWF analysis
Convergence criterion	cost function ($\chi^2 = 2S \leq \chi^2_{th}$)

AMTD
6, 6873–6933, 2013

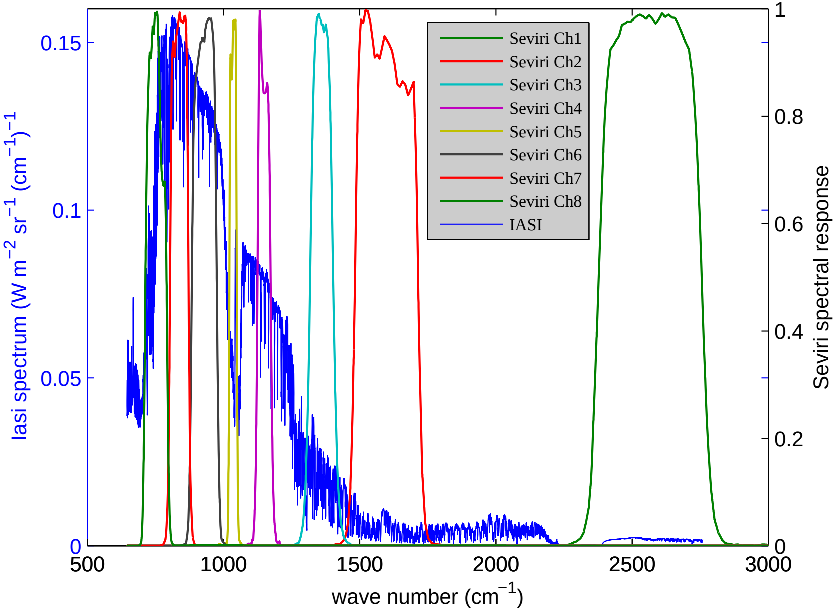

Fig. 1. SEVIRI channel spectral response over-imposed to a typical IASI spectrum.

AMTD
6, 6873–6933, 2013

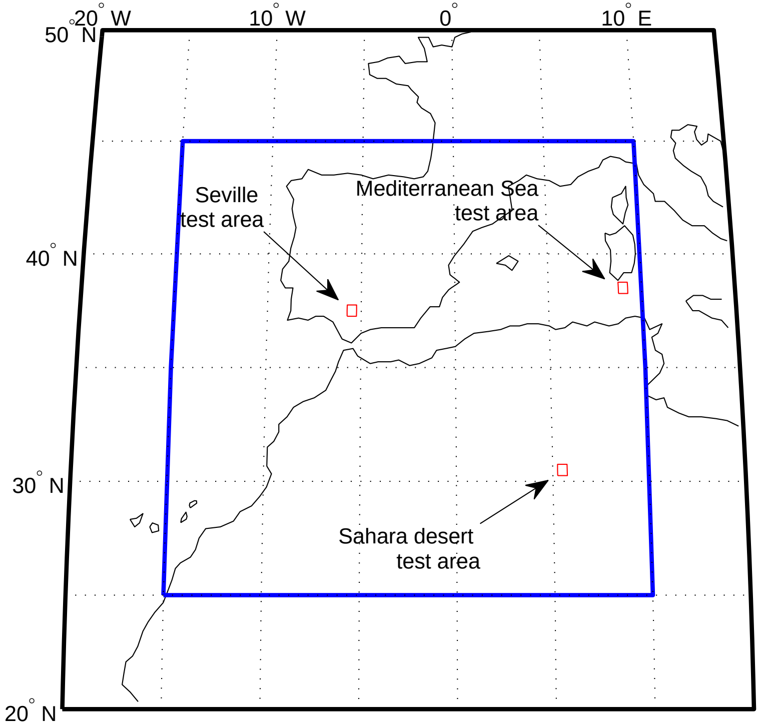

Fig. 2. Target area (rectangled in blue) used to check the retrieval algorithms. The figure also show the position of smaller test areas situated East of Seville (Spain), in a flat dune area in the Sahara desert, and below Sardinia island in the Mediterranean Sea.

AMTD
6, 6873–6933, 2013

Geophysical parameters retrieval from geostationary platforms

G. Masiello et al.

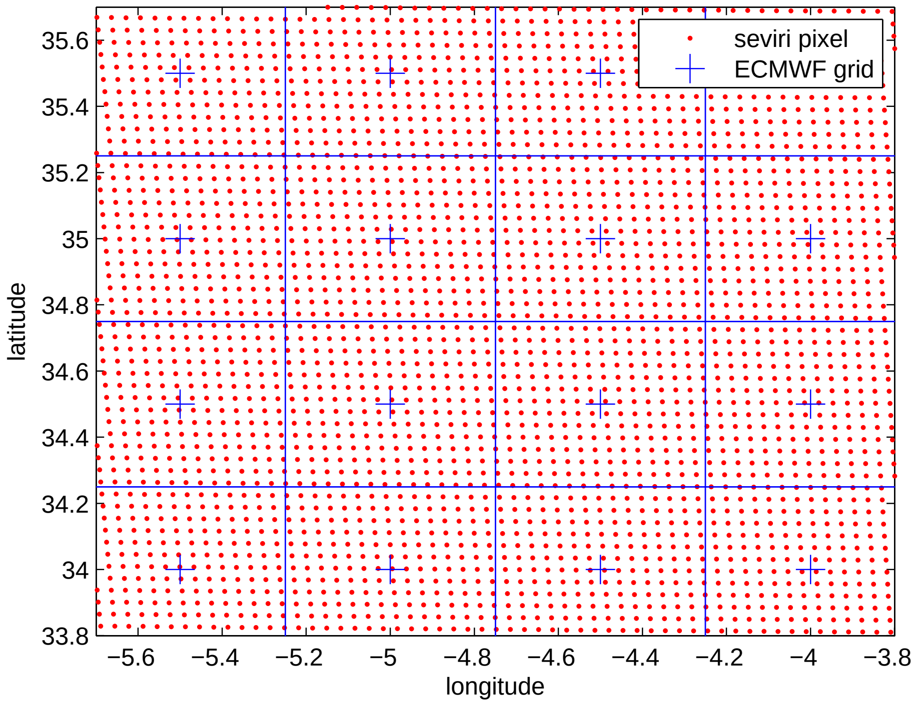

Fig. 3. Example of overlapping between the SEVIRI fine mesh and that coarse corresponding to the ECMWF analysis.

AMTD
6, 6873–6933, 2013

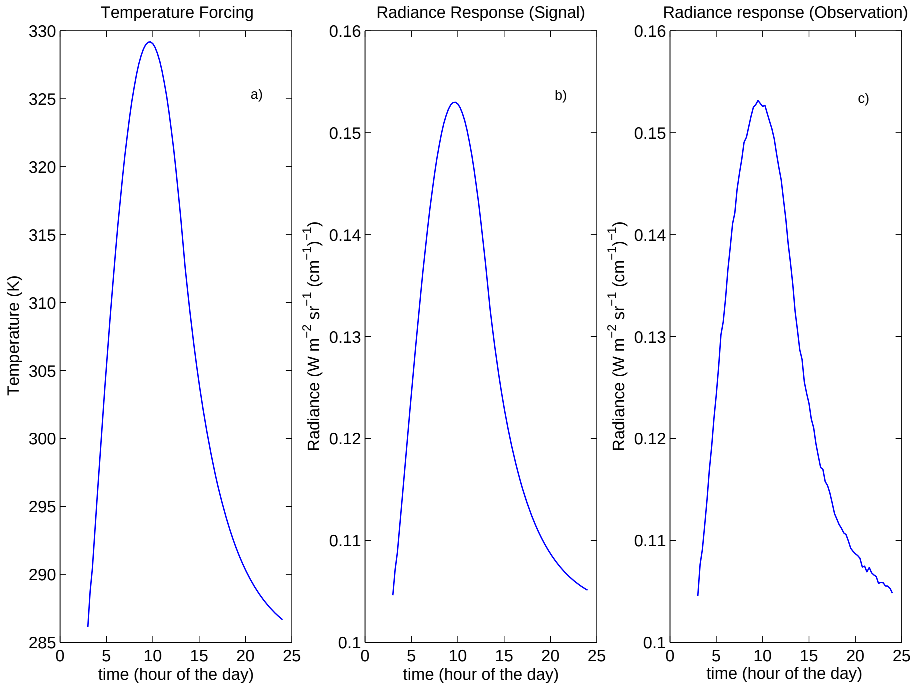

Fig. 4. Simulation of SEVIRI channel 7 (12 µm) response **(b)** to the forcing of the daily temperature cycle shown in **(a)**. **(c)** shows the effect of the SEVIRI radiometric noise over the response of **(b)**.

AMTD
6, 6873–6933, 2013

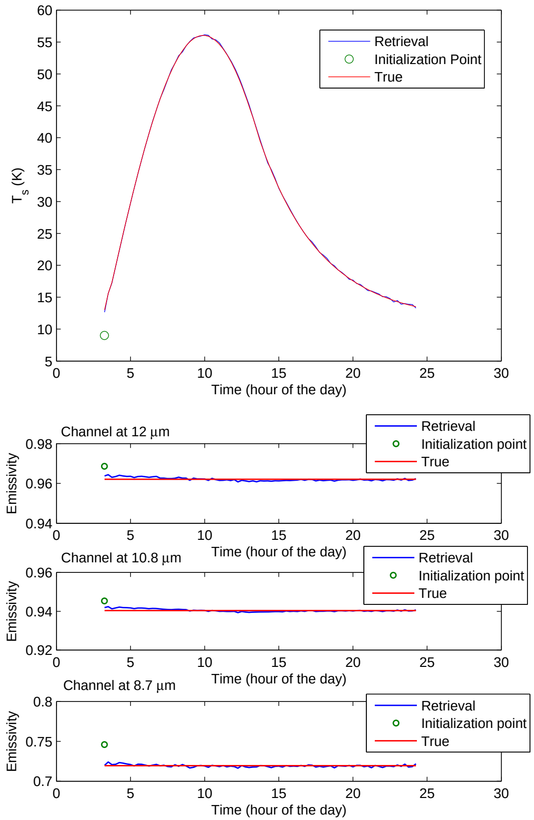

Fig. 5. Retrieval exercise in simulation with a variance of the stochastic term for T_s equal to $1\,K^2$ and $f = 10$. Upper panel: skin temperature retrieval; lower panel: emissivity retrieval at the three SEVIRI atmospheric window channels.

AMTD
6, 6873–6933, 2013

Geophysical parameters retrieval from geostationary platforms

G. Masiello et al.

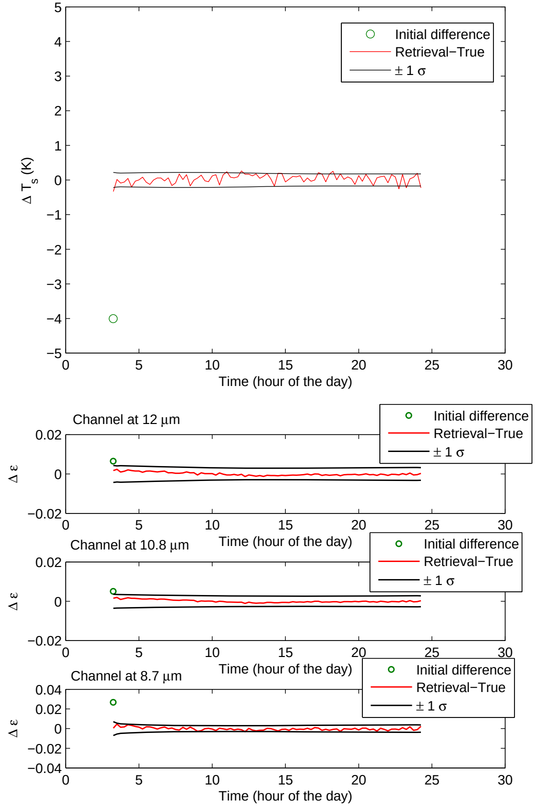

Fig. 6. Error analysis for the retrieval exercise shown in Fig. 5. The precision of the retrieval (square root of the diagonal of the covariance matrix, $\hat{\mathbf{S}}_t$) is shown in form of a $\pm 1\sigma$ tolerance interval.

AMTD
6, 6873–6933, 2013

Geophysical parameters retrieval from geostationary platforms

G. Masiello et al.

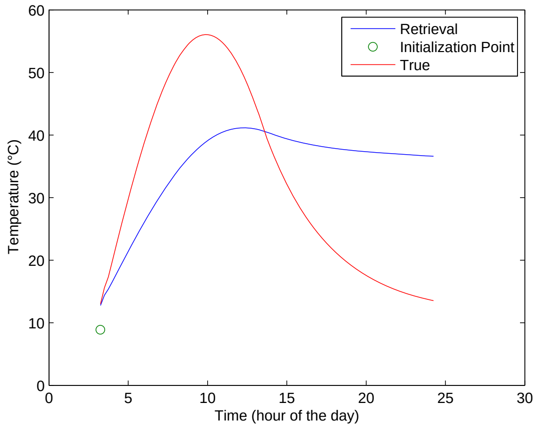

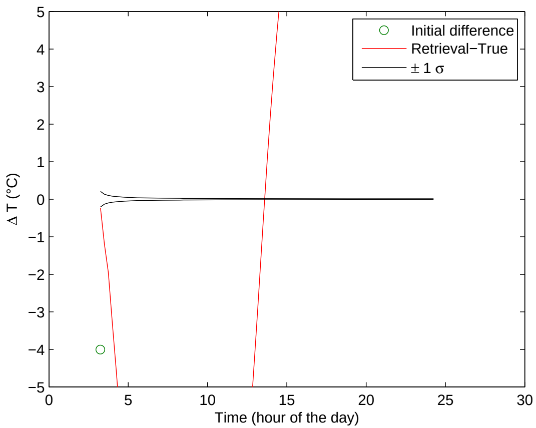

Fig. 7. Retrieval exercise similar to that shown in Fig. 5, but now the variance of stochastic term, T_s is equal to $0\,K^2$ and $f = 10$.

AMTD
6, 6873–6933, 2013

Geophysical parameters retrieval from geostationary platforms

G. Masiello et al.

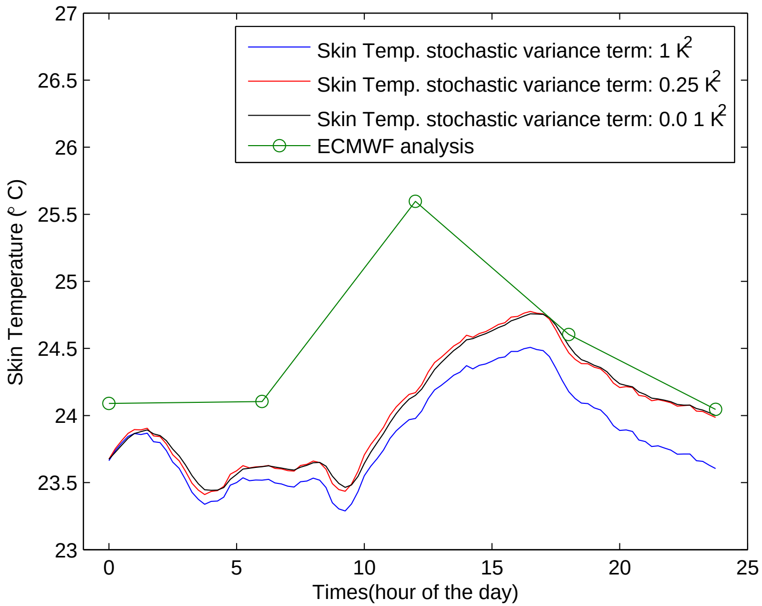

Fig. 8. Kalman filter retrieval analysis for skin temperature as a function of the stochastic variance term for T_s. The retrieval has been spatially averaged over the grid box of size 0.5° × 0.5° shown in Fig. 1.

AMTD
6, 6873–6933, 2013

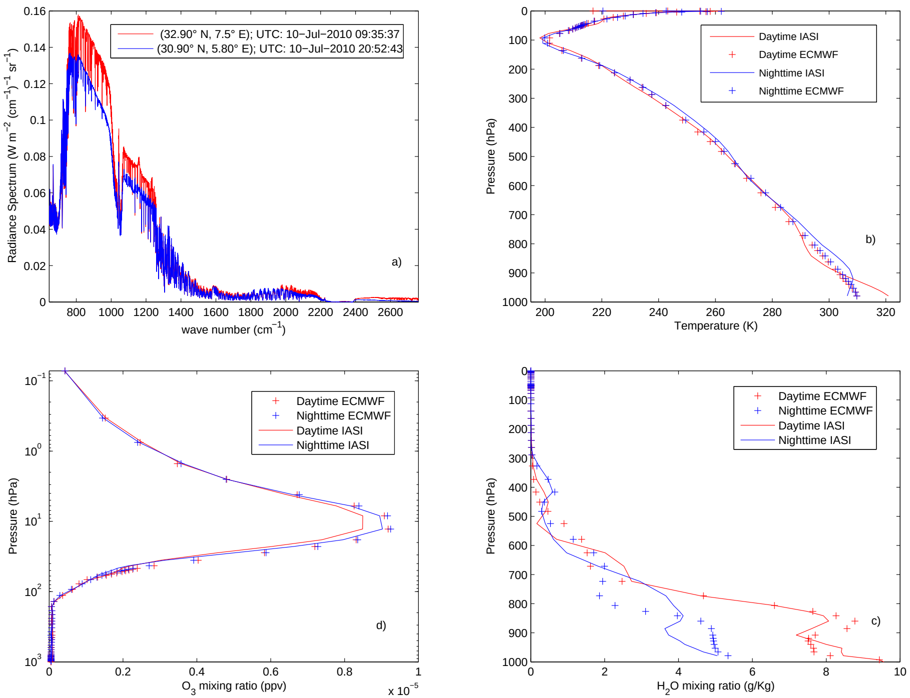

Fig. 9. (a) Day-night couple of IASI observations over a Sahara desert site; **(b)** temperature retrieval and comparison with the space-time collocated ECMWF analysis; **(c)** H_2O retrieval and comparison with the space-time collocated ECMWF analysis; **(d)** O_3 retrieval and comparison with the space-time collocated ECMWF analysis.

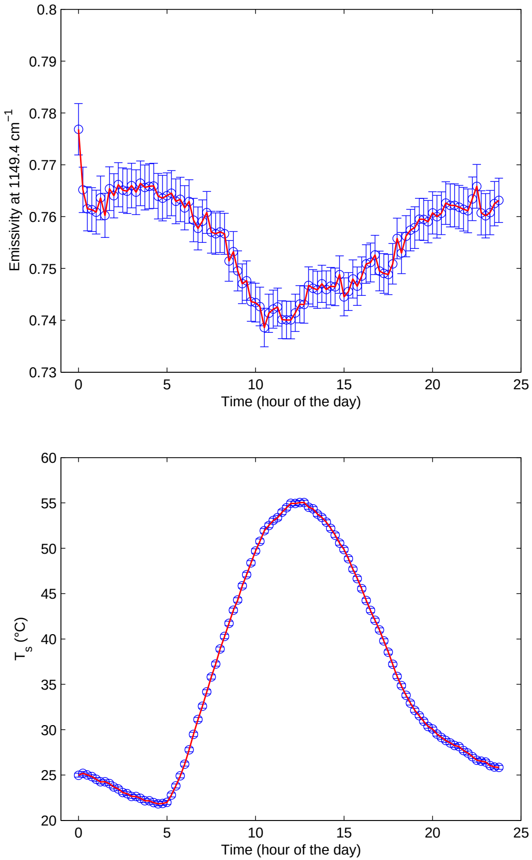

Fig. 10. Top: emissivity retrieval (channel at 8.7 µm) for one day and one single SEVIRI pixel over the Sahara desert; bottom panel: same as top, but for temperature. Error bars are the square root of the corresponding diagonal elements of the covariance matrix, $\hat{\mathbf{S}}_t$.

AMTD
6, 6873–6933, 2013

Geophysical parameters retrieval from geostationary platforms

G. Masiello et al.

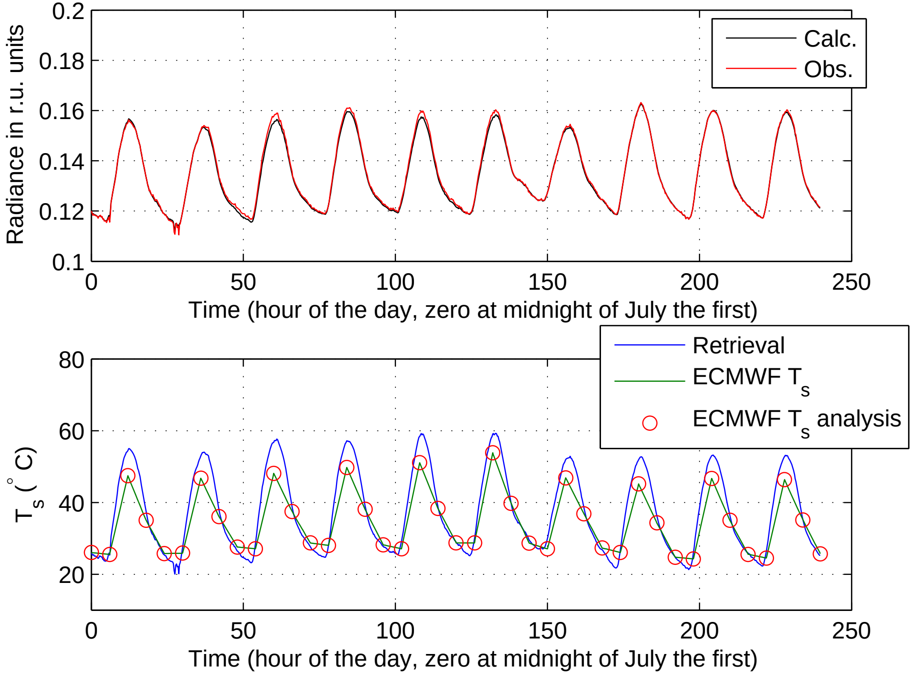

Fig. 11. Retrieved surface temperature (bottom panel) for a site in the Sahara desert. The retrieval has been obtained with the Kalman filter for ten consecutive days. In the legend, ECMWF T_s analysis refers to the surface temperature analysis at the canonical hours within a day, whereas ECMWF T_s is the ECMWF surface temperature linearly extrapolated to the SEVIRI time steps. The upper panel in the figure also shows the quality of the reconstructed radiance (channel at 12 µm). 1 r.u.=1 W m^{-2} sr^{-1} (cm^{-1})$^{-1}$

AMTD
6, 6873–6933, 2013

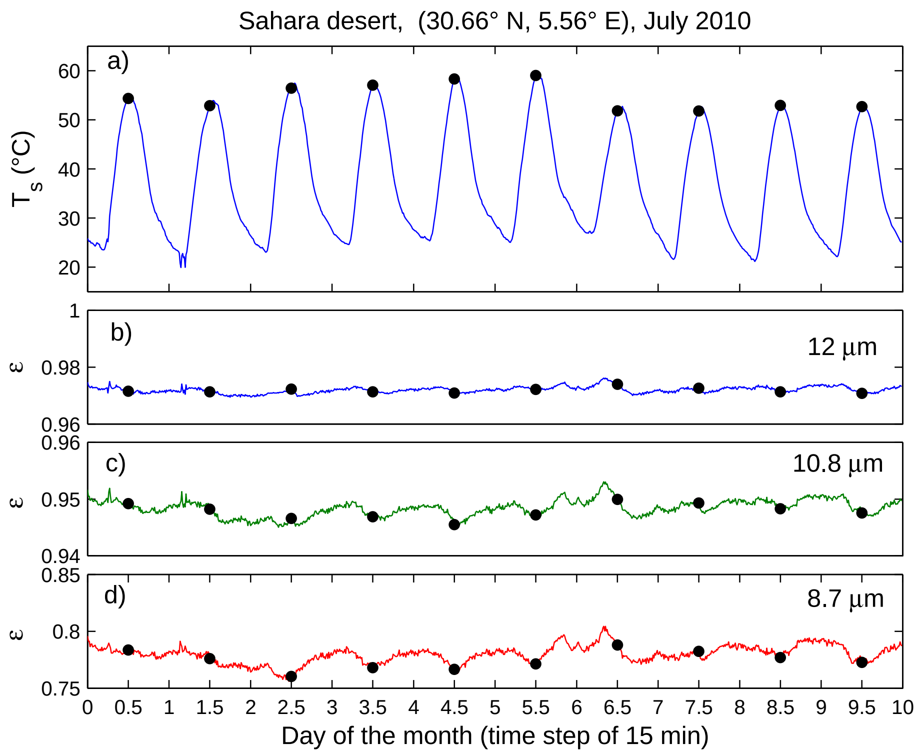

Fig. 12. $T_s - \epsilon$ time evolution for the retrieval exercise shown in Fig. 11. **(a)** Surface temperature, **(b)** emissivity at 12 µm, **(c)** emissivity at 10.8 µm, **(d)** emissivity at 8.7 µm. Black dots mark the 12:00 UTC in order to pick out the alignment of emissivity minima with noon.

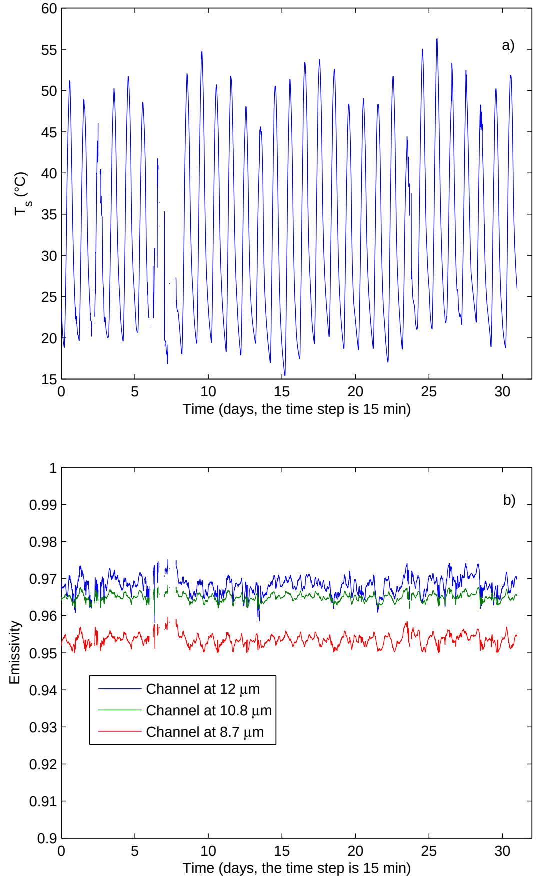

Fig. 13. Retrieved surface temperature **(a)** and emissivity **(b)** for the Seville test site. Results have been averaged over the 187 adjacent SEVIRI pixels. Only retrievals are considered, which correspond to clear sky soundings and $\chi^2 = 2S$ cost function values below threshold. Data have been processed (and are shown) at the SEVIRI repeat time of 15 min.

AMTD
6, 6873–6933, 2013

Geophysical parameters retrieval from geostationary platforms

G. Masiello et al.

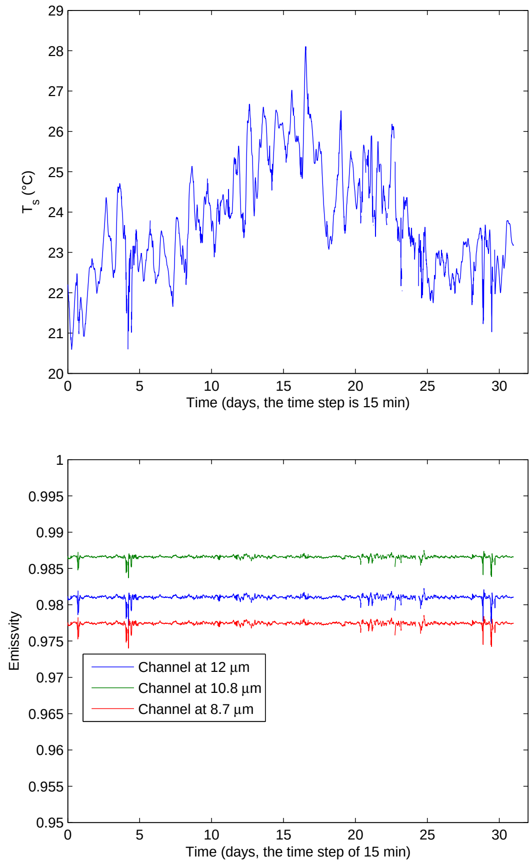

Fig. 14. Retrieved surface temperature **(a)** and emissivity **(b)** for the the Mediterranean Sea. Results have been averaged over the 178 adjacent SEVIRI pixels. Only retrievals are considered, which correspond to clear sky soundings and $\chi^2 = 2S$ cost function values below threshold. Data have been processed (and are shown) at the SEVIRI repeat time of 15 min.

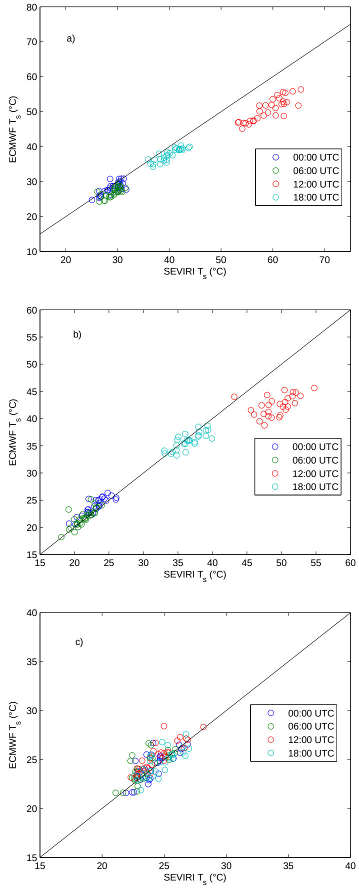

Fig. 15. Example of scatter plots of retrieved and ECMWF T_s for the three test areas. To be properly compared with ECMWF products, retrieval has been spatially averaged over the 0.5 × 0.5 grid boxes shown in Fig. 2. **(a)** Sahara desert; **(b)** Seville site; **(c)** Mediterranean Basin.

AMTD
6, 6873–6933, 2013

Geophysical parameters retrieval from geostationary platforms

G. Masiello et al.

AMTD
6, 6873–6933, 2013

Geophysical parameters retrieval from geostationary platforms

G. Masiello et al.

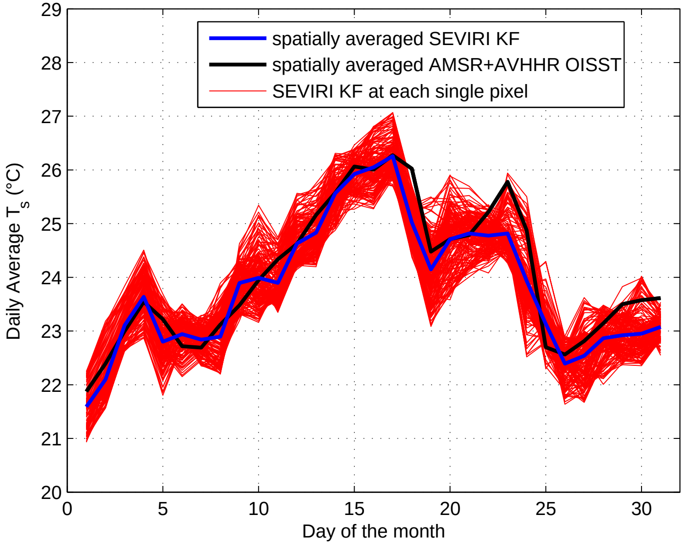

Fig. 16. Comparison of the daily average sea surface temperature retrieved with SEVIRI KF and that computed on the basis of AMSR+AVHRR OISST analysis. Each tiny red line corresponds to one single SEVIRI pixel (178 pixels in total). The two tick lines correspond to results that have been spatially averaged over the Mediterranean target area shown in Fig. 2.

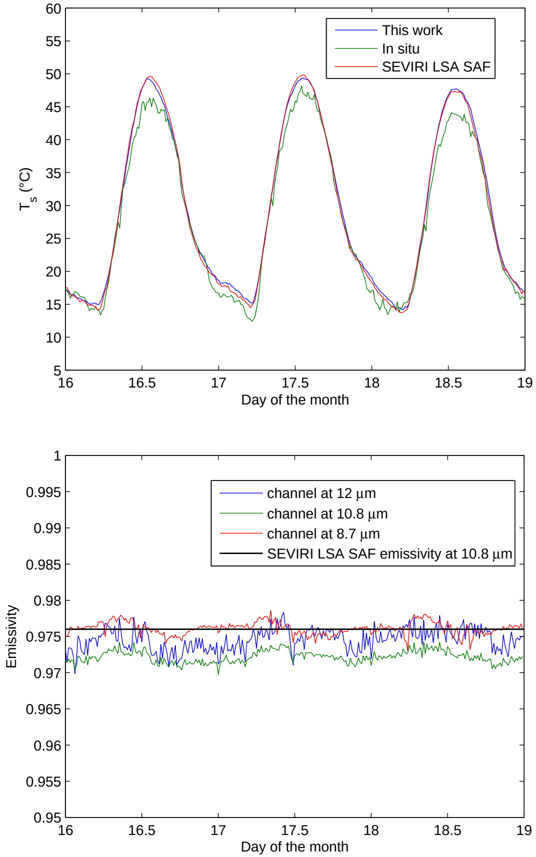

Fig. 17. Upper panel, land surface temperature for three consecutive clear sky days in July 2010 estimated according to the SEVIRI KF methodology (this work), in situ observations, and SEVIRI LSA SAF analysis. Bottom panel, KF emissivity at the three SEVIRI atmospheric window channels. For comparison the figure also shows the emissivity at 10.8 µm assumed by the SEVIRI LSA SAF analysis.

AMTD
6, 6873–6933, 2013

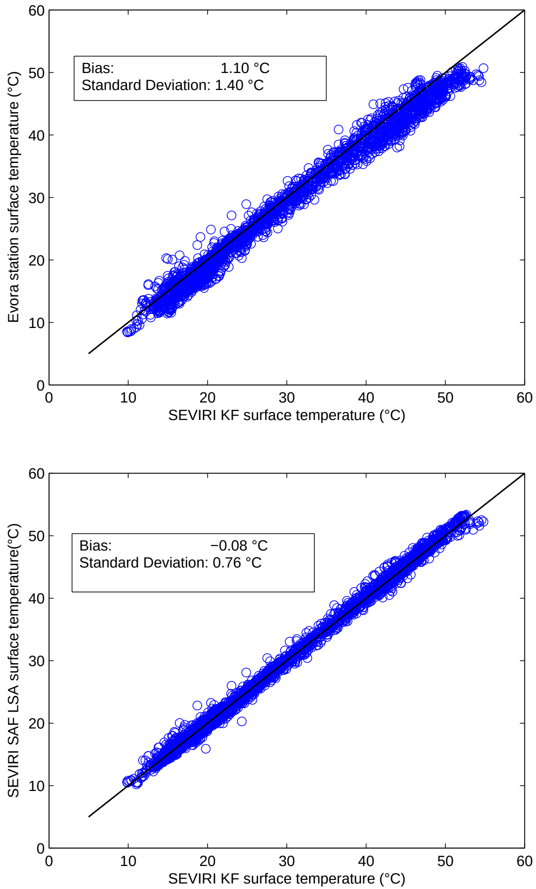

Fig. 18. Upper panel, scatter plot of $\hat{T}_s$ estimated according this work and in situ observations at Evora station. Bottom panel, scatter plot of $\hat{T}_s$ estimated according to this work and the SEVIRI LSA LST analysis.

AMTD
6, 6873–6933, 2013

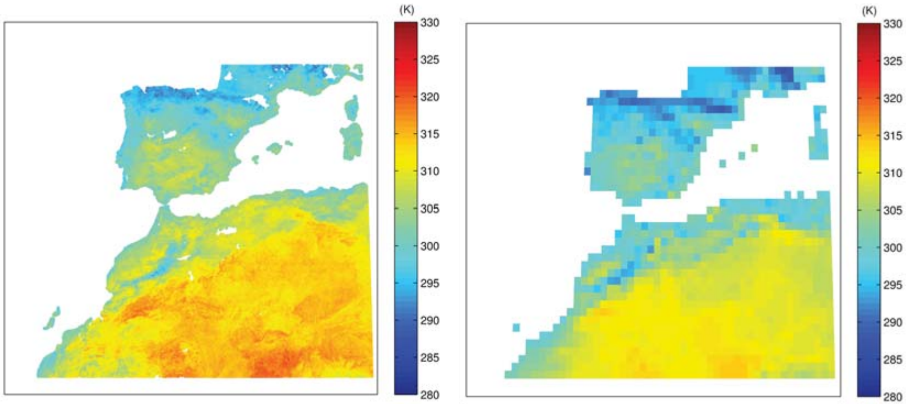

Fig. 19. Left, SEVIRI monthly map of surface temperature. Right, ECMWF monthly map of surface temperature.

AMTD
6, 6873–6933, 2013
Geophysical parameters retrieval from geostationary platforms
G. Masiello et al.

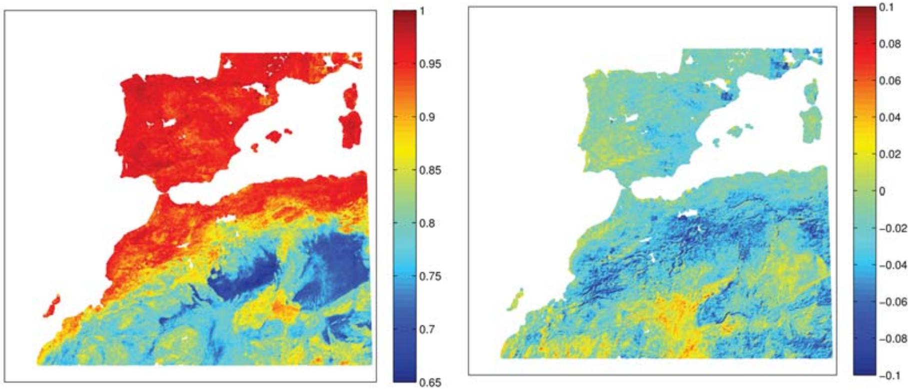

Fig. 20. Left, SEVIRI monthly map of emissivity at 8.7 µm. Right, difference with UW/BFEMIS data base for July 2010.

AMTD
6, 6873–6933, 2013

Geophysical parameters retrieval from geostationary platforms

G. Masiello et al.